THE ASTRONOMICAL JOURNAL, 117:2757–2780, 1999 June

DEEP INTERMEDIATE-BAND SURFACE PHOTOMETRY OF NGC 5907

ZHONGYUAN ZHENG,[1,3] ZHAOHUI SHANG,[1,2,3] HONGJUN SU,[1] DAVID BURSTEIN,[5] JIANSHENG CHEN,[1,3] ZUGAN DENG,[6,3] YONG-IK BYUN,[4,9] RUI CHEN,[1,3] WEN-PING CHEN,[4] LICAI DENG,[1,3] XIAOHUI FAN,[1,7] LI-ZHI FANG,[10] J. JEFF HESTER,[5] ZHAOJI JIANG,[1,3] YONG LI,[5] WEIPENG LIN,[1,3] WEI-HSIN SUN,[4] WEAN-SHUN TSAY,[4] ROGIER A. WINDHORST,[5] HONG WU,[1,3] XIAOYANG XIA,[8,3] WEN XU,[1,5] SUIJIAN XUE,[1,3] HAOJING YAN,[1,5] ZHENG ZHENG,[1,3] XU ZHOU,[1,3] JIN ZHU,[1,3] ZHENGLONG ZOU,[1,3] AND PHILLIP LU[11]

Received 1998 August 17; accepted 1999 February 16

ABSTRACT

Intrigued by the initial report of an extended luminosity distribution perpendicular to the disk of the edge-on Sc galaxy NGC 5907, we have obtained very deep exposures of this galaxy with a Schmidt telescope, large-format CCD, and intermediate-band filters centered at 6660 Å and 8020 Å. These two filters, part of a 15-filter set, are custom designed to avoid the brightest (and most variable) night sky-lines. As a result, our images are able to go deeper with lower sky noise than those taken with broad-band filters at similar effective wavelengths: e.g., 0.6 e^- arcsec^{-2} s^{-1} for our observations versus 7.4 e^- arcsec^{-2} s^{-1} for the R-band measures of Morrison et al. In our assessment of both random and systematic errors, we show that the flux level where the errors of observation reach 1 mag arcsec^{-2} are 29.00 mag arcsec^{-2} in the 6660 Å image (corresponding to 28.7 in the R band) and 27.4 mag arcsec^{-2} in the 8020 Å image (essentially on the I-band system).

In a previous paper we have shown that NGC 5907 has a luminous ring around it, most plausibly caused by the tidal disruption of a dwarf spheroidal galaxy by the much more massive spiral. Here we show that, for values fainter than 27 R mag arcsec^{-2}, the surface brightness around NGC 5907 is strongly asymmetric, being mostly brighter on the northwest (ring) side of the galactic midplane. This asymmetry rules out a halo as the cause of the faint surface brightness we see. We find this asymmetry is likely an artifact resulting from a combination of ring light and residual surface brightness at faint levels from stars that our star-masking procedure cannot completely eliminate. The possible existence of an optical face-on warp in NGC 5907, suggested by our Very Large Array H I observations, is too confused with foreground star contamination to be independently studied. Good agreement with the surface photometry of NGC 5907 by other observers leads us to conclude that their data are similarly affected at faint levels by ring light and the residual effects of star masking procedures. Inspection of published images confirm this to be the case. Thus, we conclude that NGC 5907 does not have a faint extended halo.

Key words: galaxies: individual (NGC 5907) — galaxies: interactions — galaxies: photometry — galaxies: spiral

1. INTRODUCTION

Before Sackett et al. (1994) and Morrison, Boroson, & Harding (1994, hereafter MBH) announced the discovery of a faint luminous light distribution around NGC 5907, this galaxy was primarily known as a typical edge-on Sc galaxy, which happens to be near enough to us ($V_{\rm helio} = 667$ km s^{-1} = 11 Mpc for $H_0 = 65$ km s^{-1} Mpc^{-1}) to be studied in some detail. Previous observations by several groups (e.g., Sancisi 1976; van der Kruit & Searle 1981; Skrutskie, Shure, & Beckwith 1985; Sasaki 1987; Barnaby & Thronson 1992) had shown this galaxy to have both an H I and optical warp, but no obvious galaxy companions to produce this warp. As such, NGC 5907 became the prototype of the class of spiral galaxies having "noninteracting warps" (see Sancisi 1976).

The observations of Sackett et al. (1994) sparked new interest in this galaxy, in that they claimed to detect a significant halo around it. Two other groups then obtained deep surface photometry in an attempt to study the halo in various passbands (Lequeux et al. 1996, 1998; Rudy et al. 1997). Our collaboration, the Beijing-Arizona-Taipei-Connecticut (BATC) Color Survey of the Sky (Fan et al. 1996), already had NGC 5907 as part of its galaxy calibration program. The BATC program uses the 0.6/0.9 m Schmidt telescope at the Xinglong Station of Beijing Astronomical Observatory (the "BAO Schmidt"), with its focal plane equipped with a 2048 × 2048 Ford CCD. We have custom designed a set of 15 intermediate-band filters to do spectrophotometry for preselected 1 deg^2 regions of the northern sky with this CCD system (cf. Fan et al. 1996).

Shang et al. (1998) summarize the main results of both our deep surface photometry and our Very Large Array

[1] Beijing Astronomical Observatory, Chinese Academy of Sciences, Zhongguancun, Beijing 100080, China.
[2] Department of Astronomy, University of Texas at Austin, Austin, TX 78712.
[3] Chinese Academy of Sciences–Peking University: Beijing Astrophysics Center, Beijing 100871, China.
[4] Institute of Astronomy, National Central University, Chung-Li 32054, Taiwan.
[5] Department of Physics and Astronomy, Box 871504, Arizona State University, Tempe, AZ 85287-1504.
[6] Graduate School, Chinese Academy of Sciences, Beijing 100080, China.
[7] Princeton University Observatory, Princeton, NJ 08544.
[8] Department of Physics, Tianjin Normal University, China.
[9] Center for Space Astrophysics and Department of Astronomy, Yonsei University, Seoul 120-749, Korea.
[10] Department of Physics, University of Arizona, Tucson, AZ 85721.
[11] Department of Physics and Astronomy, Western Connecticut State University, Danbury, CT 06810.

(VLA)[12] 21 cm H I observations of NGC 5907. These results are as follows:

1. We detect a faint luminous ring around the galaxy, plausibly caused by the recent tidal disruption of a nearby dwarf spheroidal galaxy.
2. The H I map picked up a companion dwarf irregular galaxy, PGC 54419, on the side of one of the H I warps, which is separated from NGC 5907 in radial velocity by only 45 km s^{-1}. As such, we move NGC 5907 out of the category of "noninteracting" warped galaxies, but whether the observed interactions are sufficient to produce the observed warp is left for galaxy modelers to decide.
3. Our H I observations suggest that the H I layer is higher near the center of the galaxy than at larger radii, suggesting that this galaxy may also have a face-on warping of the disk.

In this paper we present the details of our deep surface photometry of NGC 5907, this time paying close attention to the issue of the faint luminosity distribution around this galaxy. Section 2 presents our observations, including details of the data reduction process to enable readers to critically assess the accuracy of our method. In § 3 we study the faint luminosity distribution around NGC 5907 as it appears in our images, including how the ring, foreground stars, and a possible face-on warp can influence what we see. In § 4 we compare out results with those previously published, and we also reassess the likelihood of a halo existing around this galaxy. Section 5 summarizes the main results of this paper.

2. OBSERVATIONS AND DATA REDUCTION

The phases of data reduction contributing to errors in the final image over which we have some control are bias subtraction, dark subtraction, flat-fielding, sky background fitting, star masking, and photometric calibration. In this section we discuss these data reduction issues as they apply to the data we have obtained. Comparing our surface photometry with that of other observers in § 4, we find that, with few exceptions, our data are in very good agreement with published results.

2.1. *Data Log and Preselection of Good Images*

The observations of NGC 5907 were obtained with the BAO 0.6/0.9 m Schmidt telescope, using a thick Ford 2048 × 2048 CCD with 15 μm pixels at the f/3 prime focus. The field of view of this CCD is 58′ × 58′ and the scale is 1.″71 $pixel^{-1}$. With this combination of telescope and CCD system, we can comfortably observe large extended objects and also get a sufficient amount of sky in a single frame. A large pixel size is better for finding low surface brightness features, because it minimizes the number of CCD pixels per unit of surface area.

The images were taken with slight shifts between exposures ("dithered") so that cosmic rays and defects on the CCD could be removed during the combining process. We employed the Lick Observatory data-taking system, which automatically subtracts the overscan of each image at readout time ("on the fly"), recording the overscan in the last column. We then process each program image through a series of software routines we term PIPELINE-I, which, among other operations, median filters the original overscan and adds back to the image the difference between the original subtracted overscan and this filtered overscan. In this way, the signal-to-noise ratio (S/N) of the overscan is increased and any residual large-scale pattern produced in the image by imperfections in the overscan is removed.

Exposures of the field around NGC 5907 were made through two BATC filters: 6660 Å (m_{6660}) and 8020 Å (m_{8020}), with bandwidths of 480 Å and 260 Å, respectively (see Fig. 1 in Fan et al. 1996). The BATC filters are designed to avoid contamination by the brightest and most variable night-sky emission lines, producing a sky background of lower surface brightness than that obtainable under the same conditions in the broadband R and I filters. Using intermediate bands also minimizes effective wavelength-related effects in CCD sensitivity (§ 4.4).

A total of 137 frames of either 10 or 20 minutes' duration were obtained with the 6660 Å filter on 23 nights from 1995 January 31 to June 27, all during moonless intervals at air masses ≤ 1.5. The CCD was run with a gain of 4.1 e^- per analog-to-digital converter unit (ADU) and a readout noise of 12 e^-. Similarly, 63 frames of 20 minutes' duration were obtained with the 8020 Å filter on 11 nights from 1995 May 26 to April 18, during which time readout noise remained as before, but the gain varied somewhat. For the final combined 8020 Å image, the equivalent gain is 3.9 e^- ADU^{-1}. Of these 200 images, we selected the ones for final reduction in the following manner (see Tables 1 and 2): (1) Each individual frame was inspected visually to see if there were abnormal events that might affect photometry, e.g., traces of satellites crossing the galaxy area or visible problems with the bias overscan. If there was anything abnormal, the image was rejected. (2) For each frame we measured the mean sky level, FWHM, and flux for 20 isolated stars found in common on all frames. These values are shown in Figure 1 (and tabulated in Table 1) as a function of sequential image number for the 137 6660 Å images, with flux and sky level normalized to an integration time of 20 minutes. Those images having high stellar flux levels, low sky levels,

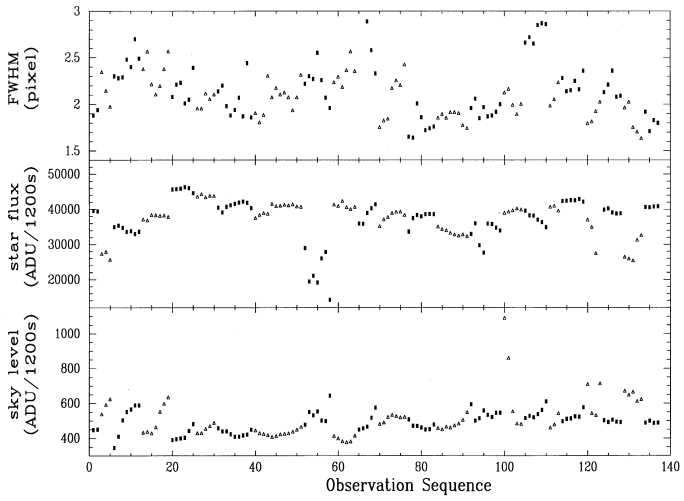

FIG. 1.—Mean values of sky level, star flux, and FWHM for 20 comparison stars found on all the frames in the 6660 Å filter. Within these parameters, we selected images with high signal-to-noise ratio to ensure that the data are as accurate as possible.

[12] The VLA is operated by the National Radio Astronomy Observatory (NRAO), which is a facility of the National Science Foundation, operated by Associated Universities, Inc.

TABLE 1

LOG OF 6660 Å IMAGES USED

Image Name[a]	Date	UT	Exposure (s)	Flux[b] (ADU)	Sky Level[c] (ADU)	FWHM Seeing[d] (pixels)
p0119803N014i019.....	1995 Mar 16	18:07:21	1200	45688.32	391.19	2.08
p0119803N014i020.....	1995 Mar 26	18:29:40	1200	45763.04	395.91	2.21
p0119803N014i021.....	1995 Mar 26	18:51:57	1200	45903.98	399.51	2.23
p0119803N014i023.....	1995 Mar 26	19:36:53	1200	46019.57	442.44	2.05
p0119803N014i024.....	1995 Mar 26	19:59:28	1200	44634.13	481.58	2.39
p0129807N014i003.....	1995 Mar 30	17:54:08	1200	43494.19	426.55	1.95
p0129807N014i005.....	1995 Mar 30	18:38:37	1200	44200.91	427.85	1.95
p0129807N014i007.....	1995 Mar 30	19:25:27	1200	43784.82	467.94	2.05
p0129808N014i009.....	1995 Mar 31	16:48:28	1200	40461.00	458.07	2.14
p0129808N014i010.....	1995 Mar 31	17:12:47	1200	39162.06	439.75	2.20
p0129808N014i011.....	1995 Mar 31	17:37:00	1200	40732.67	440.08	1.98
p0129808N014i013.....	1995 Mar 31	18:23:59	1200	41581.18	409.74	1.94
p0129808N014i014.....	1995 Mar 31	18:46:20	1200	41918.14	409.81	2.07
p0129808N014i015.....	1995 Mar 31	19:08:59	1200	42205.07	416.94	1.87
p0129808N014i016.....	1995 Mar 31	19:31:40	1200	41838.50	421.53	2.44
p0129810N014i033.....	1995 Apr 2	16:08:17	600	37385.97	442.13	1.90
p0129810N014i034.....	1995 Apr 2	16:20:45	600	38249.45	426.84	1.80
p0129810N014i035.....	1995 Apr 2	16:35:48	600	38808.16	421.85	1.88
p0129810N014i036.....	1995 Apr 2	16:49:31	600	38612.60	414.41	2.30
p0129810N014i090.....	1995 Apr 2	18:43:11	600	41381.23	405.56	2.07
p0129810N014i091.....	1995 Apr 2	18:55:39	600	40778.88	409.80	2.17
p0129810N014i092.....	1995 Apr 2	19:07:57	600	40927.23	420.08	2.10
p0129810N014i093.....	1995 Apr 2	19:20:15	600	41159.31	423.30	2.12
p0129810N014i094.....	1995 Apr 2	19:32:49	600	40996.85	424.98	2.07
p0129810N014i095.....	1995 Apr 2	19:45:06	600	41282.66	434.43	1.93
p0129810N014i096.....	1995 Apr 2	19:57:26	600	40685.38	447.11	2.07
p0129813N014i005.....	1995 Apr 5	17:33:41	1200	41198.76	410.51	2.23
p0129813N014i006.....	1995 Apr 5	17:56:09	1200	40817.11	396.47	2.29
p0129813N014i007.....	1995 Apr 5	18:20:29	1200	42195.56	380.21	2.18
p0129813N014i008.....	1995 Apr 5	18:42:52	1200	40453.31	374.80	2.36
p0129813N014i010.....	1995 Apr 5	19:28:17	1200	40533.32	412.19	2.35
p0159832N014i011.....	1995 Apr 24	16:25:51	1200	35953.96	450.15	3.33
p0159832N014i012.....	1995 Apr 24	16:49:12	1200	35878.17	456.35	3.38
p0159832N014i013.....	1995 Apr 24	17:16:16	1200	38954.00	466.10	2.89
p0159832N014i014.....	1995 Apr 24	17:39:47	1200	40301.73	517.22	2.58
p0159832N014i015.....	1995 Apr 24	18:03:18	1200	41408.85	574.39	2.33
p0159840N014i003.....	1995 May 2	16:24:05	1200	35074.59	479.29	1.75
p0159840N014i004.....	1995 May 2	16:49:06	1200	37000.46	487.52	1.82
p0159840N014i005.....	1995 May 2	17:14:12	1200	37660.10	519.02	1.84
p0159840N014i006.....	1995 May 2	17:39:27	1200	38818.73	530.52	2.17
p0159840N014i007.....	1995 May 2	18:07:31	1200	39185.15	523.33	2.25
p0159840N014i008.....	1995 May 2	18:32:47	1200	39221.22	516.27	2.20
p0159840N014i009.....	1995 May 2	18:56:33	1200	38255.55	519.34	2.42
p0159841N014i002.....	1995 May 3	16:26:44	1200	33645.56	507.71	1.65
p0159841N014i003.....	1995 May 3	16:50:30	1200	37463.91	470.97	1.64
p0159841N014i004.....	1995 May 3	17:13:39	1200	38350.46	470.50	2.01
p0159841N014i005.....	1995 May 3	17:37:20	1200	38007.07	460.79	1.86
p0159841N014i006.....	1995 May 3	18:01:55	1200	38629.03	449.87	1.72
p0159841N014i007.....	1995 May 3	18:25:25	1200	38639.90	451.50	1.74
p0159841N014i008.....	1995 May 3	18:50:47	1200	38605.21	477.84	1.76
p0169843N014i005.....	1995 May 5	15:57:59	1200	34936.81	455.66	1.85
p0169843N014i006.....	1995 May 5	16:21:19	1200	34240.71	448.46	1.89
p0169843N014i007.....	1995 May 5	16:47:35	1200	33895.24	464.00	1.85
p0169843N014i008.....	1995 May 5	17:11:23	1200	33179.18	458.11	1.91
p0169843N014i009.....	1995 May 5	17:34:57	1200	32687.67	470.84	1.91
p0169843N014i010.....	1995 May 5	17:58:08	1200	32377.79	481.40	1.90
p0169843N014i011.....	1995 May 5	18:27:31	1200	32727.70	502.62	1.77
p0169843N014i012.....	1995 May 5	18:53:45	1200	32214.26	547.08	1.74
p0169844N014i015.....	1995 May 6	17:40:14	1200	35947.07	533.51	1.87
p0169844N014i016.....	1995 May 6	18:03:27	1200	35808.12	521.69	1.88
p0169844N014i017.....	1995 May 6	18:26:38	1200	34774.71	546.38	1.92
p0169844N014i018.....	1995 May 6	18:49:34	1200	33989.09	546.47	2.00
p0179860N014i000.....	1995 May 22	14:58:24	1200	39589.11	515.46	2.66
p0179860N014i001.....	1995 May 22	15:22:14	1200	38286.74	528.31	2.72

TABLE 1—*Continued*

Image Name[a]	Date	UT	Exposure (s)	Flux[b] (ADU)	Sky Level[c] (ADU)	FWHM Seeing[d] (pixels)
p0179860N014i002.....	1995 May 22	15:46:07	1200	38195.22	520.04	2.65
p0179860N014i003.....	1995 May 22	16:10:04	1200	37075.36	538.74	2.85
p0179860N014i004.....	1995 May 22	16:35:15	1200	36371.84	562.57	2.87
p0179860N014i005.....	1995 May 22	16:58:32	1200	34934.22	611.09	2.86
p0179862N014i009.....	1995 May 24	16:36:55	1200	40573.72	458.35	1.98
p0179862N014i010.....	1995 May 24	16:59:54	1200	40855.74	476.34	2.05
p0179862N014i011.....	1995 May 24	17:22:40	1200	39471.87	540.44	2.23
p0179863N014i008.....	1995 May 25	16:00:59	1200	42368.73	497.11	2.28
p0179863N014i009.....	1995 May 25	16:23:13	1200	42437.13	511.08	2.14
p0179863N014i010.....	1995 May 25	16:45:56	1200	42616.05	513.07	2.15
p0179863N014i012.....	1995 May 25	17:30:51	1200	42919.03	523.20	2.16
p0179863N014i013.....	1995 May 25	17:53:47	1200	42156.86	577.28	2.36
p0189873N014i007.....	1995 Jun 4	15:24:25	1200	39912.96	502.76	2.13
p0189873N014i008.....	1995 Jun 4	15:48:01	1200	40254.62	492.77	2.21
p0189873N014i009.....	1995 Jun 4	16:10:39	1200	39109.38	505.35	2.36
p0189873N014i010.....	1995 Jun 4	16:45:00	1200	38815.32	493.66	2.08
p0189873N014i011.....	1995 Jun 4	17:07:40	1200	38853.51	492.20	2.09
p0209896N014i001.....	1995 Jun 27	14:13:54	1200	40678.32	488.30	1.92
p0209896N014i002.....	1995 Jun 27	14:38:33	1200	40598.48	499.05	1.71
p0209896N014i004.....	1995 Jun 27	15:30:07	1200	40878.30	488.96	1.80

[a] The image name is organized in the following sequence: prrrjjjjoooofsss, where p = PIPELINE-I processed data, rrr = run number, jjjj = Julian date (last four digits only), oooo = object number (NGC 5907 has two numbers: T514 and N014), f = filter used (i = 6660 Å, m = 8020 Å), and sss = observation sequence on the given night.

[b] Mean flux of the 20 comparison stars, normalized to 20 minute integration.

[c] Mean near-field sky level for the 20 comparison stars, normalized to 20 minute integration.

[d] Mean FWHM of the 20 comparison stars.

and reasonable seeing were selected for further study. A similar analysis was done for the 8020 Å images (Table 2), with the net result that the final combined images are made of 84 6660 Å frames taken on 15 nights and 50 8020 Å frames taken on eight nights. The total exposure time in the combined images is 26^h10^m (94,200 s) and 16^h40^m (60,000 s), respectively. The images that are used are listed in Tables 1 and 2, with their sky level counts, FWHM of stars, and the mean counts (for a 20 minute integration) measured for the 20 comparison stars.

2.2. *Bias and Dark Subtraction*

Biases measure the ADU level of zero-second exposures and, as such, are of low S/N individually. We took an average of 26 bias frames per night of observation, using the IRAF task IMCOMBINE and choosing the minmax algorithm in combination with the parameters "NLOW" and "NHIGH" set to 3 to reject bad points at the $\geq 3\ \sigma$ level. As one test of CCD stability, we take 30 bias averages from a 2 month period during the observations and divide them into two sets of 15 bias averages each: BIAS1 from the first 15 bias averages; BIAS2 from the second 15. The difference BIAS1 − BIAS2 has a mean value of zero and no large-scale pattern exists, indicating good stability of our data-taking system. The average of BIAS1 and BIAS2 (hereafter BIAS) is adopted as the final bias frame for correcting. It is equal to the average of 600 individual bias frames and has a mean value of about 1.2 ADU and a standard error of about 1 ADU pixel^{-1} (see § 2.7).

Many dark frames must also be obtained throughout the observation sequence to measure the dark current of the CCD reliably. The dark count was obtained by taking 40 20 minute dark frames over the same 2 month period. Subtracting BIAS from these frames yields a very small dark count of about 0.25 ADU pixel^{-1} per 20 minute exposure. This summed dark count frame was rescaled to the exposure time of each program image and then subtracted from each image.

2.3. *Large-Scale Homogeneity of the Program Image*

Achieving homogeneity over large scales in a CCD image requires first of all that a very accurate flat-field map of the large-scale variations that exist in CCDs. Moreover, these large-scale variations must be stable over long periods of time compared with the period during which the flat-field images and program images are obtained. To do this requires controlling two factors: (1) the DC stability of the CCD itself over the image area of interest and (2) the flatness of the night sky and twilight, which, of course, are never really flat over angles greater than 10′ (see below).

A third factor affecting the extent to which the sky can be subtracted from the image of a galaxy concerns the quantum efficiency (QE) of a CCD pixel, which is a function of the effective wavelength of the radiation it detects. The one part of the data-taking process we *cannot* control is that the galaxies have different spectral energy distributions (SEDs) within the filters and that these SEDs are different from that of the night sky.

While we cannot completely eliminate systematic effects on the large-scale homogeneity of any of these factors, we have taken steps to minimize their influence as follows.

1.—*DC stability*: We can comfortably fit a galaxy as large as NGC 5907 (14′ in diameter) within the inner 25% of the CCD, which itself is in the inner 20% of the field of a Schmidt telescope. This eliminates concerns pertaining to edge-effects in CCD flat fields and minimizes nonuniformity issues related to the optics of the telescope.

2.—*Flatness of the flat fields*: On a CCD chip covering essentially $1^\circ \times 1^\circ$ of the sky, neither the twilight nor the night sky will be flat over the whole chip (Wild 1997). This is

TABLE 2

LOG OF 8020 Å IMAGES USED

Image Name[a]	Date	UT	Exposure (s)	Flux[b] (ADU)	Sky Level[c] (ADU)	FWHM Seeing[d] (pixels)
p0330135N014m039.....	1996 Feb 21	19:02:58	1200	27634.88	506.71	2.09
p0330135N014m040.....	1996 Feb 21	19:26:01	1200	27828.17	474.49	2.15
p0330135N014m041.....	1996 Feb 21	19:48:33	1200	27768.68	453.67	2.03
p0330135N014m042.....	1996 Feb 21	20:11:05	1200	27738.37	421.46	1.96
p0330135N014m043.....	1996 Feb 21	20:33:50	1200	28107.29	395.21	1.97
p0330136N014m036.....	1996 Feb 22	17:17:53	1200	27405.63	436.15	1.91
p0330136N014m037.....	1996 Feb 22	17:41:21	1200	27723.22	454.58	1.90
p0330136N014m038.....	1996 Feb 22	18:03:50	1200	27836.49	462.55	1.94
p0330136N014m039.....	1996 Feb 22	18:26:24	1200	27933.66	439.44	1.92
p0330136N014m040.....	1996 Feb 22	18:49:04	1200	27979.31	405.05	1.88
p0330136N014m041.....	1996 Feb 22	19:11:39	1200	28081.59	414.47	1.90
p0330136N014m042.....	1996 Feb 22	19:34:13	1200	28007.59	393.42	1.93
p0330136N014m043.....	1996 Feb 22	19:56:38	1200	28007.20	383.90	1.92
p0330136N014m044.....	1996 Feb 22	20:19:11	1200	28133.33	415.54	2.03
p0330136N014m045.....	1996 Feb 22	20:41:35	1200	28087.49	402.87	2.17
p0330141T534m038	1996 Feb 27	19:07:08	1200	24137.61	550.05	2.38
p0330141T534m039	1996 Feb 27	19:29:47	1200	24496.86	589.32	2.26
p0330141T534m040	1996 Feb 27	19:52:35	1200	24779.54	623.50	2.26
p0330141T534m041	1996 Feb 27	20:15:21	1200	24840.06	671.74	2.23
p0330141T534m042	1996 Feb 27	20:38:05	1200	24996.80	654.99	2.29
p0340153N014m035.....	1996 Mar 10	18:32:29	1200	26708.87	749.01	2.30
p0340153N014m036.....	1996 Mar 10	18:55:00	1200	26668.87	703.19	2.29
p0340153N014m037.....	1996 Mar 10	19:17:42	1200	26710.86	683.35	2.57
p0340153N014m038.....	1996 Mar 10	19:40:54	1200	26759.61	749.38	2.39
p0340153N014m039.....	1996 Mar 10	20:03:40	1200	26791.77	764.89	2.23
p0340153N014m040.....	1996 Mar 10	20:26:10	1200	26821.89	778.71	2.16
p0340157T534m042	1996 Mar 14	17:52:54	1200	22775.84	520.57	2.40
p0340157T534m043	1996 Mar 14	18:15:20	1200	23111.24	544.43	2.43
p0340157T534m044	1996 Mar 14	18:37:57	1200	22794.46	560.05	2.46
p0360190N014m002.....	1996 Apr 16	16:33:07	1200	31314.58	438.65	2.42
p0360190N014m003.....	1996 Apr 16	16:56:39	1200	31275.79	480.01	2.38
p0360190N014m004.....	1996 Apr 16	17:20:21	1200	31147.07	484.32	2.48
p0360190N014m005.....	1996 Apr 16	17:44:13	1200	31053.15	477.52	3.19
p0360190N014m006.....	1996 Apr 16	18:08:19	1200	31111.32	482.44	3.11
p0360190N014m008.....	1996 Apr 16	19:00:01	1200	30521.54	359.35	3.41
p0360190N014m009.....	1996 Apr 16	19:23:44	1200	30067.63	420.39	2.41
p0360191N014m020.....	1996 Apr 17	17:00:54	1200	29464.94	414.97	1.98
p0360191N014m021.....	1996 Apr 17	17:24:51	1200	29541.54	353.81	2.38
p0360191N014m022.....	1996 Apr 17	17:48:24	1200	29756.01	330.02	1.68
p0360191N014m023.....	1996 Apr 17	18:13:53	1200	29926.16	312.84	1.70
p0360191N014m024.....	1996 Apr 17	18:36:24	1200	30251.59	313.91	1.81
p0360191N014m025.....	1996 Apr 17	18:59:09	1200	30290.93	335.49	1.84
p0360191N014m026.....	1996 Apr 17	19:21:42	1200	30314.27	333.15	1.96
p0370192N014m024.....	1996 Apr 18	16:49:22	1200	29078.35	581.85	1.89
p0370192N014m025.....	1996 Apr 18	17:11:48	1200	29211.13	552.14	1.77
p0370192N014m026.....	1996 Apr 18	17:34:31	1200	28949.63	516.00	1.67
p0370192N014m027.....	1996 Apr 18	17:57:22	1200	29204.02	531.85	1.82
p0370192N014m028.....	1996 Apr 18	18:21:37	1200	29693.29	572.58	1.99
p0370192N014m029.....	1996 Apr 18	18:44:10	1200	29669.82	545.97	1.84
p0370192N014m030.....	1996 Apr 18	19:06:46	1200	28722.99	590.20	2.05

[a] The image name is organized in the following sequence: prrrjjjjoooofsss, where p = PIPELINE-I processed data, rrr = run number, jjjj = Julian date (last four digits only), oooo = object number (NGC 5907 has two numbers: T514 and N014), f = filter used (i = 6660 Å, m = 8020 Å), and sss = observation sequence on the given night.

[b] Mean flux of the 20 comparison stars, normalized to 20 minute integration.

[c] Mean near-field sky level for the 20 comparison stars, normalized to 20 minute integration.

[d] Mean FWHM of the 20 comparison stars.

obvious upon visual inspection of the twilight sky, when one considers that the field of view of our CCD is twice the size of the full Moon. Moreover, airglow brightness correlates with air mass, to which anyone who has done photometry can attest. Even on a cloudless, moonless night our eyes can detect airglow brightness gradients over degree-sized scales anywhere in the sky. One might be able to devise a methodology of taking night-sky flats at various air masses and in various sky directions to minimize gradients in the night sky, but such techniques are likely to be very time consuming and offer no guarantee that sky gradients can be completely eliminated.

Instead, we take advantage of the special optical properties of a Schmidt telescope to construct a reliable flat-fielding method that can make use of a dome light. As detailed in Chen et al. (1999), we place a UV-transparent plastic diffuser over the correcting lens of the Schmidt. One dome light flat-field frame has more than 20,000 ADU pixel^{-1}, corresponding to more than 84,000 electrons (gain = 4.1). Twelve dome flats produce an overall flat field whose statistical pixel-to-pixel error is less than 0.1%. The diffuser ensures that the flux entering the Schmidt telescope is of a highly uniform nature. In the present paper, the proof of the accuracy of this flat-fielding technique is demonstrated in two ways: by comparing noise in the division of average flat fields taken on successive nights with that expected from photon noise alone and by the accuracy with which we can flatten the sky.

3.—*Color-related effects*: One consideration prompting our decision to use intermediate-band filters for the BATC survey is the fact that SED-related QE effects do exist in CCDs. Our own tests with stars (see Fan et al. 1996) show the measurements made in the two filters used here are insensitive to color changes in the program objects at the 1% level. Such is not necessarily the case for observations made with broadband filters (Stetson 1990).

2.4. *Rectification of the Summed Image*

After the correction for the flat field was applied, we calculated position offsets among the selected CCD frames with six plate coefficients, taking into consideration the position of the frame center, using the positions of stars in the Guide Star Catalog of the Space Telescope Science Institute (Lasker et al. 1990). This process is performed during the PIPELINE-I reduction process, and the derived plate coefficients are put into the FITS image header. After shifting all corrected images to a common center, bad pixels and cosmic rays are rejected and the cleaned images are combined to a single frame. We then redetermine the plate coefficients and plate center for the combined frames. The net images in the 6660 Å and 8020 Å filters contain 1928 × 1969 pixels and 1979 × 1979 pixels, respectively. Figure 2*a* shows the combined image in the 6660 Å filter; Figure 2*b* shows the combined image in the 8020 Å filter.

2.5. *Prediction of Background under the Galaxy and Ring*

A reliable estimate of surface brightness at faint levels near NGC 5907 requires us to be able to reliably determine the sky background in the regions of interest. These include not only the regions immediately adjacent to NGC 5907, but also the ring that we found around it. This, in turn, means modeling the background formed not only by the night sky, but also by extraneous sources of light, including stars, other galaxies, and, if present, Galactic "cirrus."

2.5.1. *Star and Galaxy Masking*

The stars and background galaxies to be subtracted on the combined image range from faint, near–point-sources of light to large regions contaminated by highly saturated stars. The traditional way to handle these sources of extra light is to mask them until their wings fall under a certain level, say, 10% of the variation in the sky. This is the procedure followed by MBH and Lequeux et al. (1996). We found that following this procedure with our own combined images would leave us with too few sky pixels from which to determine a reliable sky background. As a result, we proceed in a different, stepwise manner.

First, using DAOPHOT (Stetson 1987), we fitted a point-spread function (PSF) to each combined image. The fitted PSF is then subtracted from star images that are not saturated, following the prescription given in the 1987 Stetson paper and in the DAOPHOT II User's Manual. Saturated stars were not subtracted. Key to this process is as accurate a subtraction of the wings of the PSF as one can practically make.

The next step is to check the reliability of the PSF subtraction by plotting the residuals (obs − PSF model) versus distance from PSF center for each unsaturated star. The PSF wings are subtracted cleanly for most stars and there is little remnant. However, the central areas of these subtracted stars show higher statistical fluctuations than the wings, owing to the higher original signal in the centers. While circular masks are placed over the stars in such cases, the circles cover far less area than they would have if the PSF wings of every star had been masked in their entirety.

The brightest, unsaturated stars form an exception to this second step, because PSF subtraction leaves a noticeable residual at faint light levels. Therefore, we treat the brightest stars, whether saturated or unsaturated, the same, masking out the whole star to faint, but finite sky levels. In total, 117 bright stars in the 6660 Å image were masked in this way.

Other galaxies that are resolved on our images are easily found via the DAOPHOT star subtraction process, because the PSF subtraction leaves a deficit of flux at the galaxy center surrounded by a bright halo. All background galaxies are masked entirely, but they are generally so faint that these mask radii are small.

Figure 3 shows four results of the PSF subtraction, including a saturated star, a bright unsaturated star fitted by the PSF, a faint star fitted by the PSF, and a faint galaxy fitted by the PSF. The vertical lines indicate the masking radii used. Our tests on all PSF-subtracted stars show that the residuals of the PSF fits are less than 5 ADU on average, or approximately 5% of the statistical *noise* of the sky.

Treating saturated stars in these images is more problematic. In principle, the images of stars that cannot be PSF-fitted because of saturation effects should be wholly masked. Unfortunately, as stated earlier, if we tried to completely mask every bright star in our image, we would not be left with many pixels left in the image! As a result, we are forced to make two compromises in our star-masking procedure. First, we only mask each bright star to a surface brightness of 29 mag arcsec^{-2}. Second, because of the optics of a Schmidt telescope, the PSFs of the stars are not symmetric anywhere in focal plane of our telescope. This is easily seen in Figures 2*a* and 2*b* of the present paper. However, the masks are, by necessity, symmetric. The net result is a slight mismatch of mask and PSF at very low light levels. As we will see, these compromises limit what we can do at faint light levels around NGC 5907.

In our 6660 Å combined image, there are 7921 unsaturated objects detected, among which are 1694 background galaxies in 1000 × 1000 pixels (1710″ × 1710″). We also note that, if one compares our 6660 Å combined image with Figure 2 of MBH and Figure 1 of Sackett et al., it is clear that our observation is as deep, if not deeper, than theirs, detecting all of their stars plus some fainter stars.

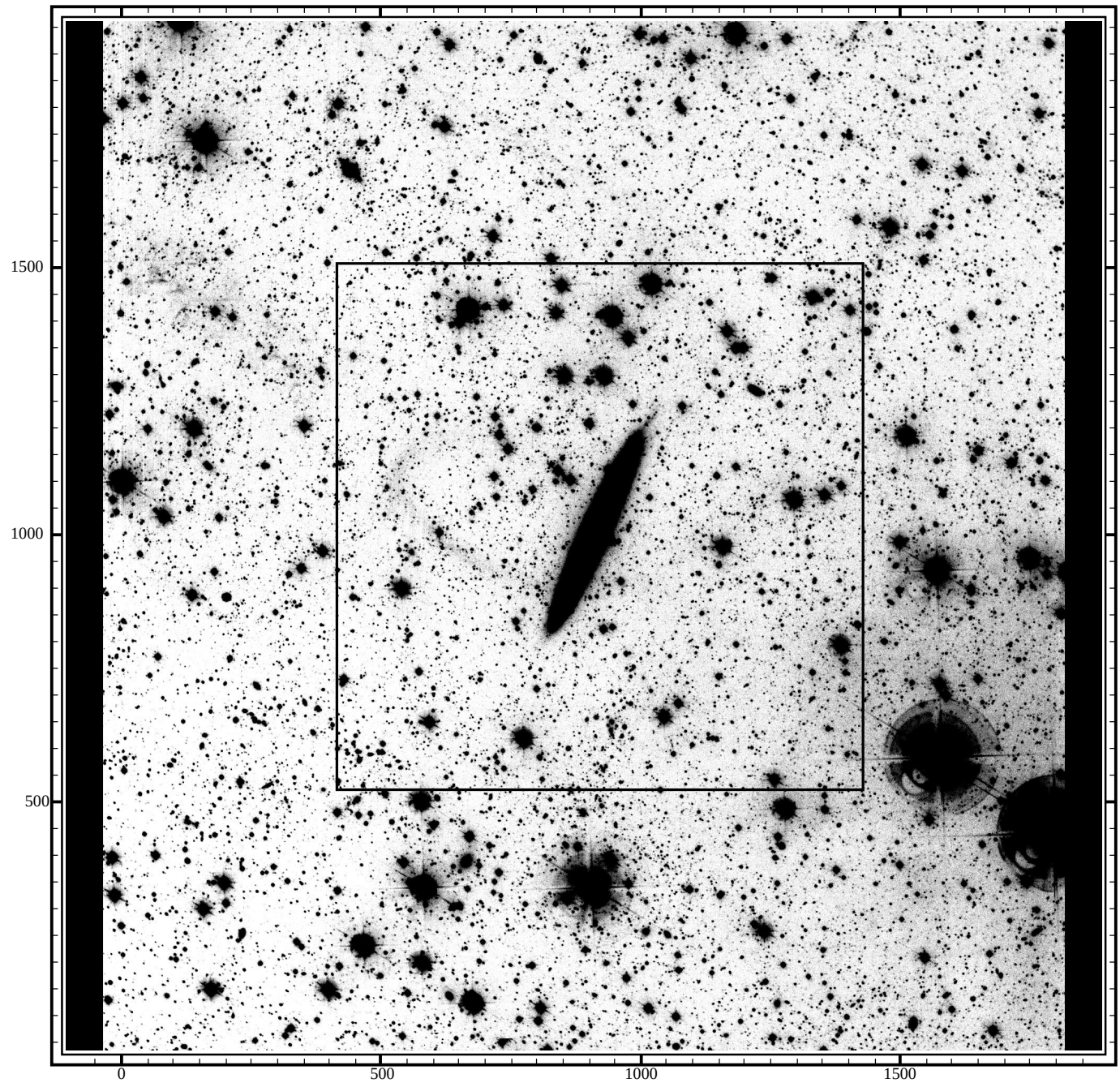

FIG. 2*a*

FIG. 2.—(*a*) Combined deep image of NGC 5907 at 6660 Å, 26^h20^m. The central square (1000 × 1000 pixels) shows the area used in our photometry. The ring around NGC 5907 can be seen faintly in this image; its mean 6660 Å surface brightness is 28 mag arcsec^{-2}. (*b*) 8020 Å, 16^h40^m combined image of NGC 5907. Note that the surface brightness of the ring is too faint to be seen in this image.

Quantitatively, our detection threshold is 3.5 σ_{sky}, resulting in a limited magnitude of 23.3. This means that for $m_{6660} \leq 23.30$, $\log N_{star} = 4.45$ deg^{-2} and $\log N_{galaxy} = 3.88$ deg^{-2}. Star counts are overestimated and galaxy counts are underestimated, because galaxies that are unresolved appear stellar and galaxies with too low surface brightnesses are not found.

Separately, we mask out a circle with a radius of 250 pixels around the galaxy, as well as an area around the ring that is otherwise not excluded. This procedure ensures that no galaxy- or ring-related flux is included in the sky background determination, but it also means that the residual flux from bright stars masked in these regions is not modeled. The final masked 6660 Å image is shown in Figure 4.

2.5.2. *Sky Background Fitting*

Once star and galaxy masking is complete, we can attempt to model the sky background. Because it only makes sense to do this calculation near the galaxy and ring, we can safely limit ourselves to the inner 1000 × 1000 pixel areas (28′.5 × 28′.5) in each combined image, the region

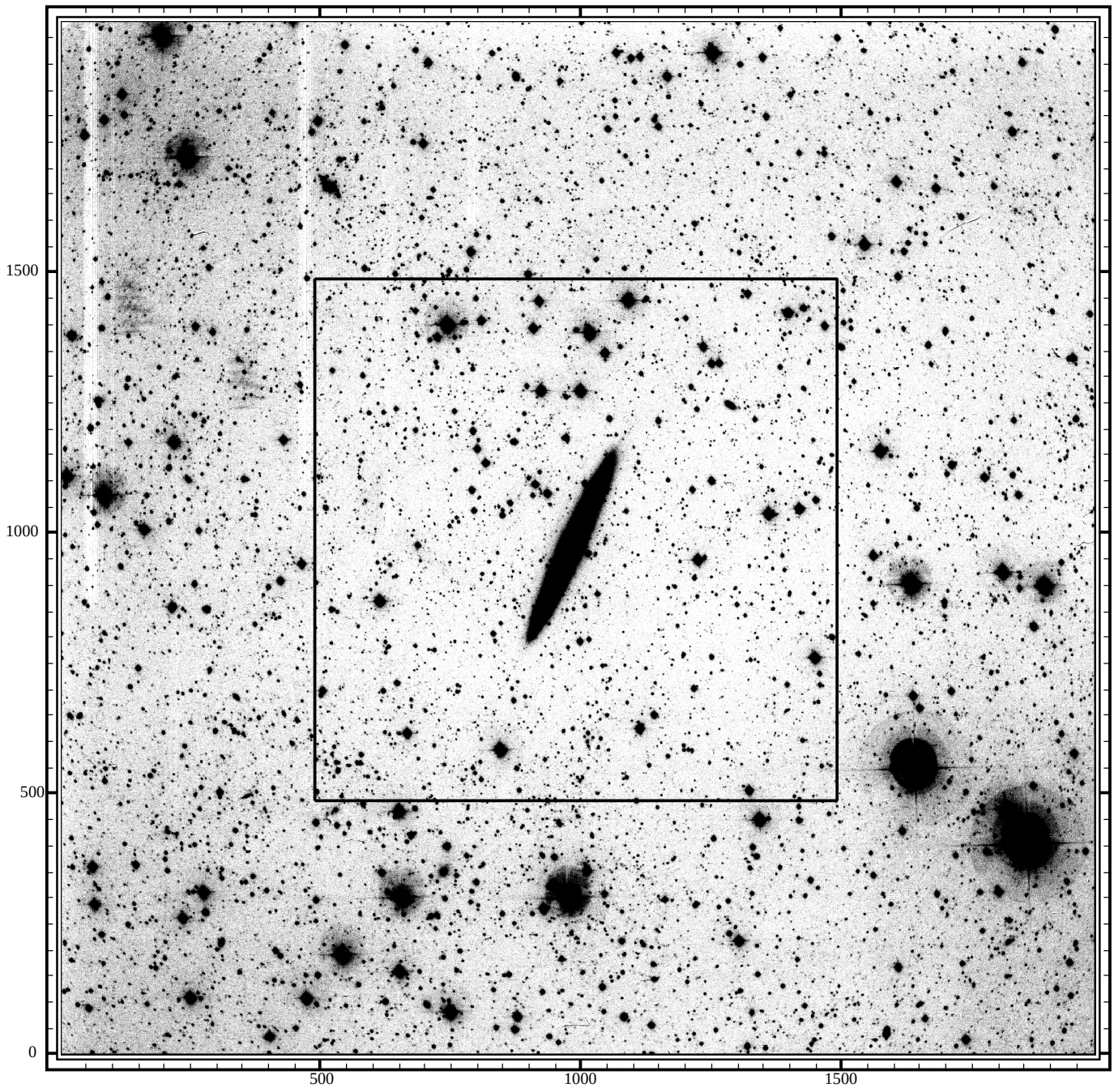

FIG. 2*b*

marked by the square in Figure 2*a*. This is also the region defined by our masking procedure (Fig. 4).

First, we produced a smoothed version of each masked combined image by mode filtering each image with a box 10×10 pixels in size. To avoid contamination by masked pixels, only those pixels not in a masked area were used in calculating the mode in any box. This necessarily meant that fewer pixels were used to generate the mode near each masked region. After smoothing, the masked regions with radii larger than the box size are shortened and those with radii smaller than the box size disappear. Once this smoothing operation is done, the original mask is reimposed on the image, thus eliminating the pixels located in original masked areas. As a result of this process, edge effects from the masking procedure are removed.

We next experimented with the IRAF task IMSURFIT to perform sky background fitting with various two-dimensional analytic functions. None of these models was found to be wholly satisfactory, because we had to restrict the fits to low-order polynomials to avoid introducing spurious interpolations in the masked regions. In every case, we could see large areas of the image that were systematically underfitted or overfitted. Low-order spline fits similarly suffer. In the end, we settled on a stepwise method that works reasonably well with a large part of the image masked out.

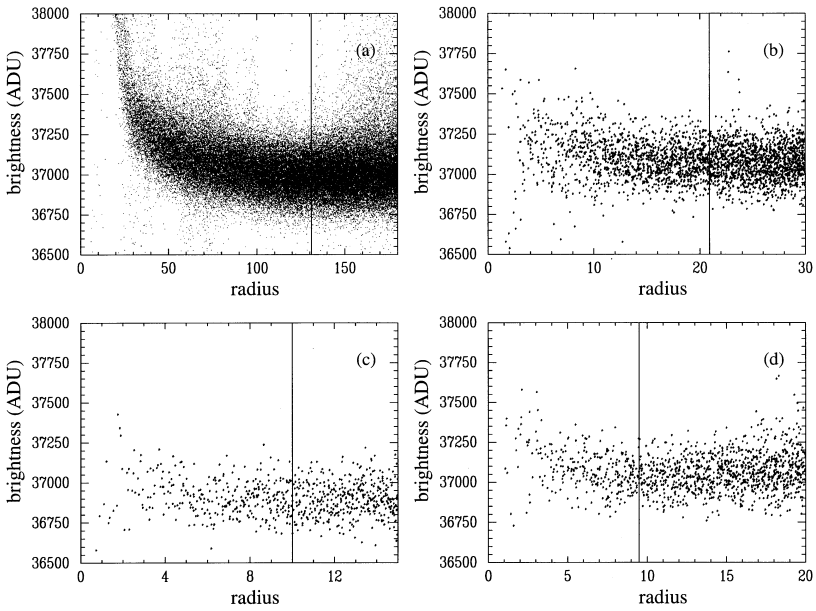

FIG. 3.—Four examples of subtracting and masking stars and galaxies. (*a*) Saturated bright star. This PSF cannot be subtracted by DAOPHOT. Its wing extends so far that the mask radius is larger than 130 pixels. Another saturated star is found near this one. Their mask circles exclude most contamination of their extended wings. (*b*) Unsaturated bright star. The residuals after the PSF is fit show that the central pixels have large fluctuations around the sky level, and the residual wing of its PSF is still partly visible. The mask radius used is 21 pixels. (*c*) Star of moderate brightness. The residuals after PSF is fit show significantly smaller variation in its center than for the bright star, and the PSF wings for this star are smaller as well. The mask radius used is 10 pixels. (*d*) Faint galaxy. The PSF for a galaxy is much more gradual than that of stars, such that it cannot be subtracted properly by DAOPHOT using a stellar PSF. The mask radius used is 9 pixels, while a star with the same brightness requires a mask radius of only 5 pixels or less.

We fitted each row of the smoothed and masked image with a one-dimensional Legendre polynomial of low order. In doing this fit, we reject points above 2 σ on the high side and 3 σ on the low side, as well as all pixels inside the mask. The reason for the asymmetric rejection of points is that the main sources of scatter on the high side are faint, undetected sources and unfitted faint wings of stars, while the low-side values result from statistical fluctuations. This is clearly seen when histograms are made of the pixel values in the masked images; the histograms are skewed toward positive values. This process necessarily requires the interpolation of each line under the galaxy/ring mask, holding the order of the Legendre polynomial to 3 or less.

The row fit to the smoothed 6660 Å image is shown in Figure 5*a*. Next, we repeat this process in the column direction (Fig. 5*b*). This ensures that we are predicting the sky underneath the galaxy in a mutually orthogonal manner. The row and column fits are then averaged (Fig. 5*c*), and this average image is smoothed with a circular Gaussian of $\sigma = 30$ pixels, truncated at $\pm 4\,\sigma$. The final smoothed image was adopted as the sky background (Fig. 5*d*).

The 6660 Å image with its fitted background subtracted is shown in Figure 6*a*, and the 8020 Å image is shown in Figure 6*b*. As is evident, even with our best attempt at star subtraction and masking, faint, partial rings remain visible near many of the brighter stars. These rings are at surface brightnesses of 29 mag arcsec^{-2} and fainter in the 6660 Å image. As stated earlier, this end result is a compromise, for if we were to truly exclude all starlight from this image, very little would be left of the image from which to determine sky in many of the MBH cuts, leaving little net flux to examine in these cuts. NGC 5907 is obviously located at a Galactic latitude (51°) where stellar crowding starts to have serious effects on what one can be accomplished quantitatively at low surface brightnesses. As a check of the accuracy of our background fitting and masking procedures, we have taken four averages of 30 rows ("slices") each through the background-subtracted 6660 Å image (Fig. 7) and the similarly processed 8020 Å image (Fig. 8) that span the region of interest around NGC 5907.

These sky-subtracted slices through the galaxy are given at the top of each panel in Figures 7 and 8. At the bottom of each panel appear the residuals of the subtracted sky background for each slice. The upper line is the residual of our sky fitting and subtracting procedure, while the lower line is the residual of normal two-dimensional function fitting. They are shifted down by 110 ADU and 150 ADU, respectively, for display purposes. It is obvious that our procedure produces smaller residuals than two-dimensional function fitting. Figures 7 and 8 can be used by readers to check whether our sky subtraction procedure introduces any spurious features into the sky-subtracted image. The lower parts of these panels also demonstrate that our sky subtraction procedure conservatively fits an effective two-dimensional plane under the masked region around the galaxy.

Of course, no sky background fit is perfect, and these imperfections help put limits on the accuracy of faint surface photometry. To estimate the systematic error from this source, we sampled 381 areas of 50 × 50 pixels of the background-subtracted 6660 Å image and calculated the mode value of each area. After excluding areas in the region severely affected by masking, the standard error of these mode values is 18 ADU. We take this as our best estimate of the irreducible 1 σ accuracy of our sky background fit. In a similar manner, we determined the accuracy of the sky background fit to be 17 ADU for the 8020 Å image.

In contrast, when we limited our sky background fits exclusively to those obtained by analytical two-dimensional functions, the row slices showed many more systematic variations and the 1 σ systematic error was typically 30 ADU. We believe our method of sky background fitting

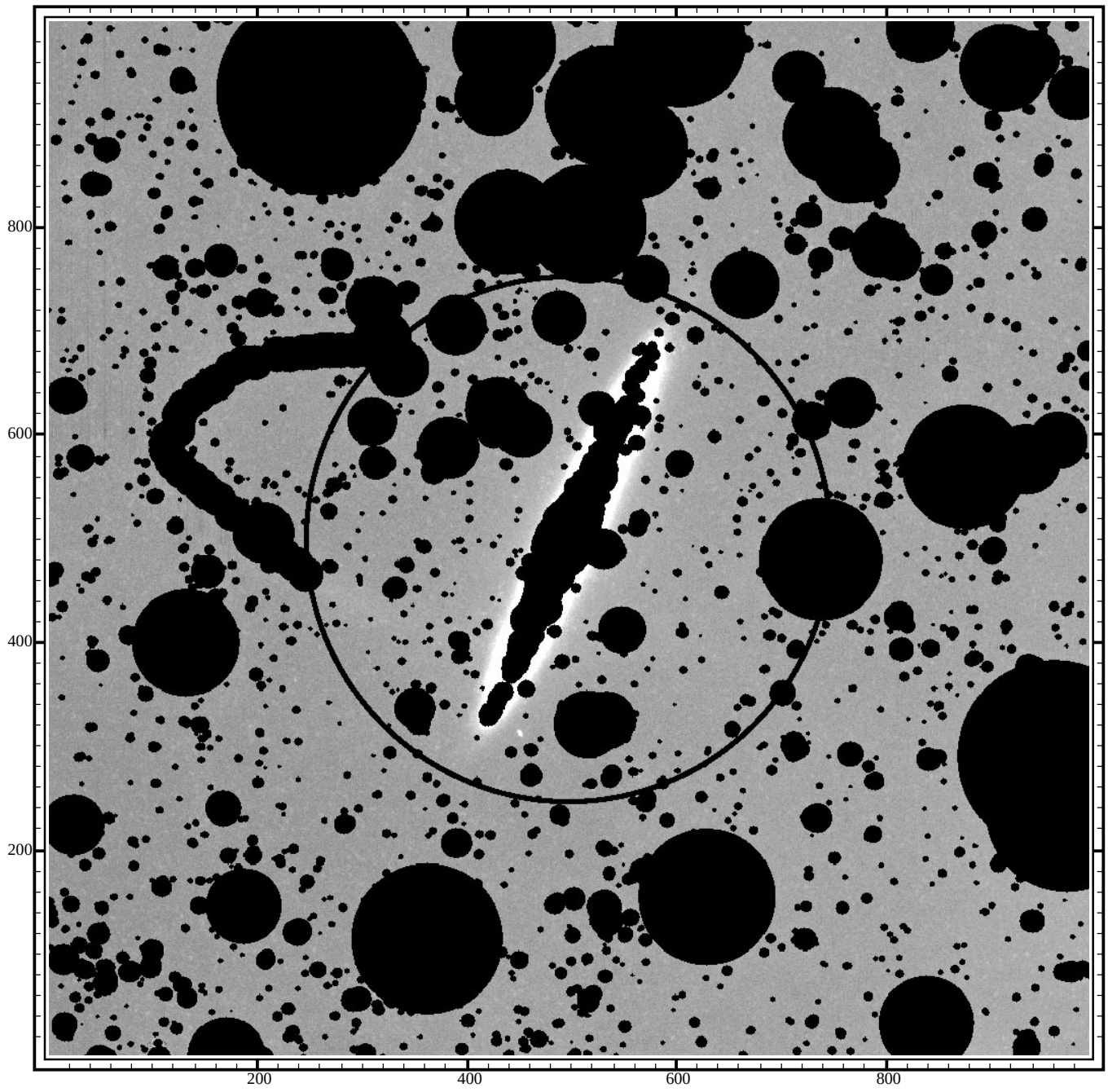

FIG. 4.—Final mask to be applied to the 6660 Å image to account for foreground stars and background galaxies and a circular region around NGC 5907. The central circle indicates the region in which all pixels around NGC 5907 are masked; the curved area around this circle masks the ring we found around this galaxy. Separately, for profile determinations the dust lane of NGC 5907 is also masked. The mask radii of most faint stars are too small and low in contrast to be clearly displayed in this image.

produces a reliable match to what is inherently a very lumpy sky at very low light levels.

2.6. *Zero-Point Calibration*

When the night is photometric, it is standard practice for BATC observations to use Oke & Gunn (1983) standard stars as calibration stars. The nights of 1995 March 6 and 1996 April 1 in the series taken for NGC 5907 were photometric. The magnitude zero point for each combined image corresponding to a flux of 1 ADU s^{-1} is 19.08 ± 0.01 mag for the 6660 Å image and 17.79 ± 0.01 mag for the 8020 Å image. The sky brightness values are 21.26 mag arcsec^{-2} and 19.91 mag arcsec^{-2}, respectively. The parameters we derive for these two combined images are given in Table 3. Note that the FWHM of the PSF of the combined images (2.3 and 2.5 pixels, or 2″ in radius) is worse than the typical seeing of 2″ at the Xinglong Observation Station of the Beijing Astronomical Observatory using the Schmidt telescope (see Fig. 1).

2.7. *Estimated Errors We Can Control*

The random error per pixel is given by the random error in photoelectrons, not in ADU. In the case of the 6660 Å image, there are 4.1 e^- ADU^{-1} and 3.9 e^- ADU^{-1} for the

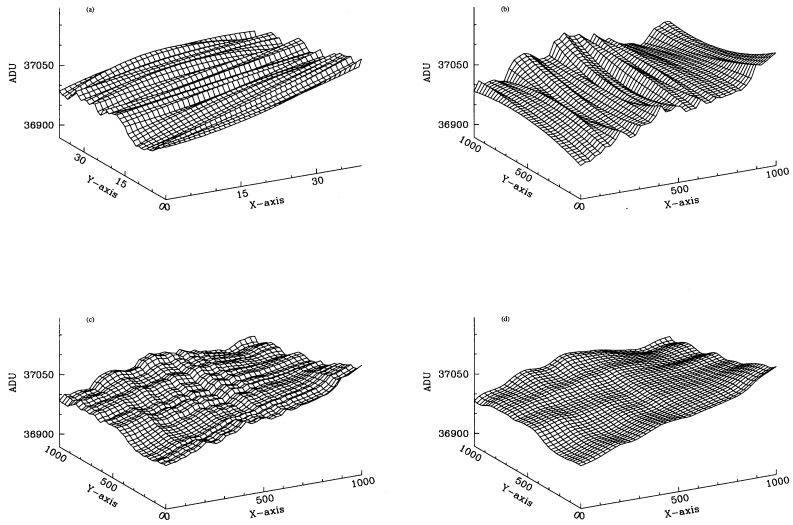

FIG. 5.—Four steps of background fitting. (*a*, *upper left*) Image is fitted row by row with Legendre polynomials of order 3 or less. (*b*, *upper right*) Image is fitted column by column in the same way. (*c*, *lower left*) Average of (*a*) and (*b*) is taken. (*d*, *lower right*) Gaussian function used to smooth (*c*). The final fitted background is too complicated to be expressed by any two-dimensional analytical function. The net results of the fit underneath the galaxy region are shown in the slices in Fig. 7 and Fig. 8.

8020 Å image. Hence, if a pixel has n ADU, this corresponds to $4.1n$ e^- for the 6660 Å image and the error is $(4.1n)^{1/2}$ in e^-, equivalent to an error of $(n/4.1)^{1/2}$ in ADU. In the case of the 8020 Å image, the error would be $(n/3.9)^{1/2}$. The sources of error in our images we can estimate are readout noise, photon noise per pixel, noise in average bias, noise in average dark, noise in flat-fielding, and systematic errors in sky background mapping. Note that all of these noise levels except for two (systematic flat-fielding errors and systematic sky background errors) can be reduced by increasing the number of pixels sampled.

Readout noise.—Random noise from readout comes from a readout noise (in terms of error of the mean) of 12 e^- pixel^{-1} per image. In the case of the 6660 Å combined image (84 input images), this is $12 \times 84^{1/2} \approx 110\, e^-$ pixel^{-1}, and $12 \times 50^{1/2} \approx 85\ e^-$ pixel^{-1} for the 8020 Å image (50 input images). From above, the noise in the readout is 26.8 ADU pixel^{-1} for the 6660 Å image and 21.8 ADU pixel^{-1} for the 8020 Å image.

Photon noise.—Photon noise per pixel is given simply as $4.1^{1/2}$ ADU for the 6660 Å image and $3.9^{1/2}$ ADU for the 8020 Å image.

Bias and dark.—Because the ADU per pixel counts of average bias and dark are very small, the main error of 3 ADU pixel^{-1} comes from the readout noise. The final bias image used for bias subtraction was an average of 600 single bias frames, resulting in a noise of 0.12 ADU pixel^{-1}. The error transmitted into the combined image in 6660 Å is $0.12 \times 84^{1/2} \sim 1$ ADU pixel^{-1}. The error introduced by dark subtraction is also about 1 ADU pixel^{-1} for both passbands. Compared with the photon noise of night sky and readout noise of the program images, the errors introduced by biases and darks are thus negligible.

Flat-fielding.—As is evident from Figures 7 and 8, our flat-fielding procedure produces a flat enough image for the structure in the background to be dominated by the intrinsic lumpiness of the faint night sky. This result is consistent with the tests we performed to confirm the validity of our flat-fielding procedure (Chen et al. 1999). However, from the flat field we do have some pixel-to-pixel noise as a result of photon statistics. For each filter, 12 frames of dome flat fields, each with more than 20,000 ADU, are combined together to make the final flat-field image. Thus, the photon noise in the flat field is $(20{,}000/4.1)^{1/2}/12^{1/2} \sim 20$ ADU, or 0.1%. Since the final galaxy image was combined from 84 dithered frames, the error was reduced by $1/84^{1/2}$ to 0.01%, approximately. For the 8020 Å image, it is about 0.015%.

Given the changes in flat-field pattern night to night and run to run in a typical CCD system, we performed separate checks of the large-scale uniformities of our flat fields by dividing the combined flat-fielding frame of one night by that of the adjacent night. Nine divisions of flat fields taken in the 6660 Å band have an average pixel-to-pixel variation of 0.16%, indicating that the noise of the combined flat-fielding frame of one night is about 0.11%. This value is consistent with the 0.1% predicted by calculating photon noise, showing that our flat fields are very stable from night to night. Because these divisions also included any large-

TABLE 3

PARAMETERS OF THE COMBINED IMAGES

Filter (Å)	Total Exposure Times	FWHM Seeing[a] (pixels)	Sky Level (mag arcsec^{-2})	σ_{sky}^{b} (ADU)	Readout Noise[c] (e^-)	Zero Point[d] (ADU s^{-1})
6660.....	26^h10^m	2.3	21.26	105	110	19.08
8020.....	16^h40^m	2.5	19.91	85	85	17.79

[a] Mean FWHM of all the stars in the field.
[b] Standard error of sky background per pixel.
[c] Total readout noise introduced into final combined images per pixel.
[d] Photometry zero point calibrated by measuring Oke-Gunn standard stars.

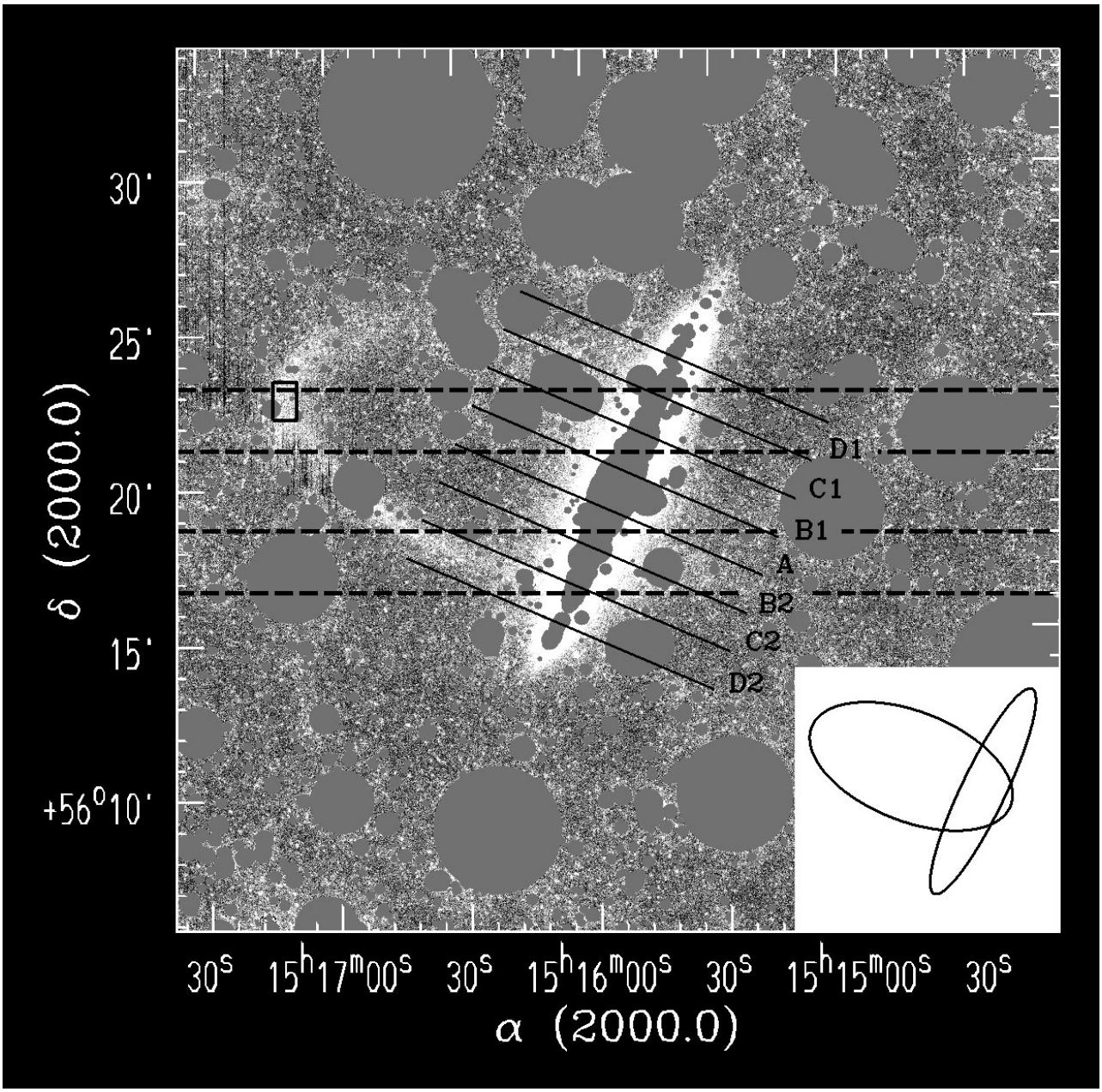

FIG. 6*a*

FIG. 6.—(*a*) Background-subtracted image at 6660 Å. The ring around the galaxy is very clear. It is a near-perfect but not complete ellipse, with a major axis of 13.7, minor axis of 7.2, and eccentricity $e = 0.84$ (see Shang et al. 1999). The major-axis size is 44 kpc at a predicted distance of 11 Mpc (assuming $H_0 = 65$ km s^{-1} Mpc^{-1}). The area within the rectangle marked in the image was measured to determine the average surface brightness of the brightest area of the ring at 6660 Å and 8020 Å, so that we can get color index of the ring with reasonable accuracy. A schematic figure is inserted in bottom right corner of the image to show the relative position of the ring and the galaxy. The solid lines with labels indicate the cuts along which surface photometry of the galaxy halo is done. These cuts are the same as those of Sackett et al. (1994) and MBH. The dashed lines show the centers of the slices made to check effect of background subtraction. Note the extent to which foreground stars exist to affect the surface brightness distributions we can obtain in the MBH cuts. (*b*) Background-subtracted image in 8020 Å.

scale pattern changes in the flat field, the test also shows that the large-scale pattern is reproduced very accurately with the dome/diffuser technique for a Schmidt telescope. When we then smooth the flat-field ratios by binning up pixels, we find that large-scale variation is about 0.026%. Therefore, the large-scale error of the combined flat-fielding frame of one night is slightly less than 0.02%.

Intrinsic variation in galaxy brightness.—MBH point out that the intrinsic variation could be expressed by the formula given by Tonry & Schneider (1988), assuming $\overline{M}_R = 0$ (Tonry, Ajhar, & Luppino 1990). In our case, $m_1 = 19.08$ mag, the exposure time is 94,200 s, and the distance is 11 Mpc (assuming $H_0 = 65$ km s^{-1} Mpc^{-1}). Because the central wavelength of our 6660 Å band is similar to that of the *R* band and the difference between our 6660 Å band and the *R*-band magnitude is small (§ 4.1), a value of $\overline{M}_{6660} = 0$ is a reasonable assumption. This gives an estimated variance of $3.3g$, where g is the mean number of counts due to exclusively to the galaxy. Thus, 45 ADU pixel^{-1} (equal to 28.5 mag arcsec^{-2}) will yield an error of 12 ADU pixel^{-1},

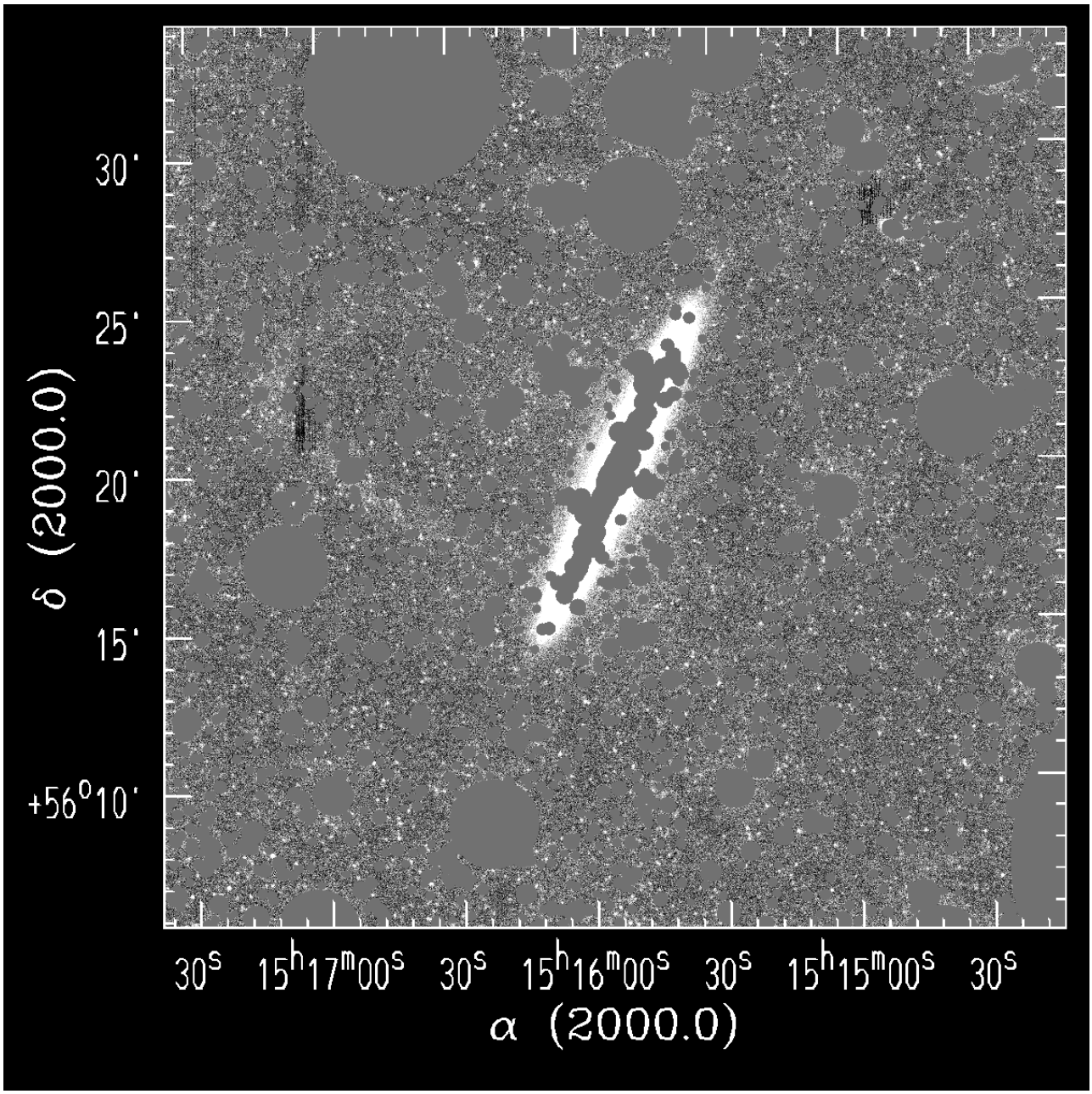

FIG. 6*b*

far less than the night-sky photon noise of 95.1 ADU pixel^{-1}. The estimated variance of the photon noise in the 8020 Å image is 1.6*g*, assuming $\overline{M}_{8020} \sim -1$, when $\overline{M}_R \sim 0$ and $\overline{M}_I \sim -2$ (Tonry et al. 1990). For 22 ADU pixel^{-1} (equal to 27.5 mag arcsec^{-2}) we get an error of 6 ADU pixel^{-1}, small compared with our other sources of random error.

2.8. *Total Error Budget*

Random noise.—Of the photon noise resulting from the night sky, readout noise, bias/dark count errors, and random flat-fielding errors, the reducible random errors in a blank sky area are dominated by the first, and we estimated them to be close to 100 ADU pixel^{-1} for the 6660 Å image and 83 ADU pixel^{-1} for the 8020 Å image. These figures are roughly consistent with the σ measured directly from the combined images (see Table 3). These noises and intrinsic galactic variation can be reduced by binning adjacent pixels. As the distance from the galaxy plane increases, the bin size increases exponentially to maintain a similar S/N. For example, with a bin size of 45 × 59 pixels at the farthest distance, the random noise is reduced to only 2 ADU.

Large-scale flat-fielding error.—According both to our own tests described above and those made by Chen et al. (1999), the large-scale error of BATC flat-fielding is less than 0.1%. Since we combined 84 frames for the 6660 Å band and 50 frames for the 8020 Å band, the error introduced by this source is reduced to about 0.01%.

Systematic error in background subtraction.— In the previous section we found that the irreducible scatter in the images is 18 ADU for the combined 6660 Å image and 17 ADU for the combined 8020 Å image. Taken together with

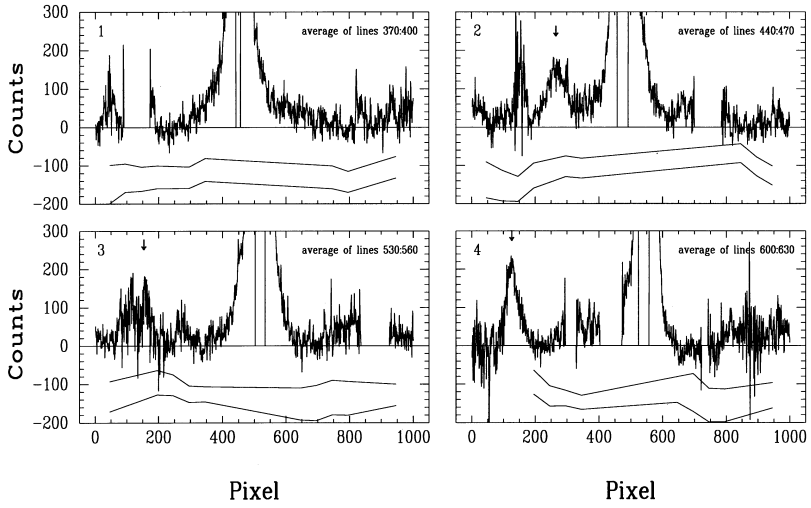

FIG. 7.—Four slices of the background-subtracted 6660 Å image to show the accuracy of background fitting and local surface brightness of the ring feature. The positions of the center of each slice relative to the galaxy and ring are represented in Fig. 6*a* by the dashed lines. Each slice is averaged over 31 lines of the image, and only nonmasked pixels are averaged. If all 31 points are masked, a zero value is assigned. Also shown are straight lines indicating the zero level. Note the small, but still apparent, residual effect of our star subtraction/masking procedure, a product of the compromise made in the star-masking procedure. The lower part of each panel (below the zero lines) shows the residuals of subtracted sky background for each slice. The upper line in this part of each panel shows the residuals produced by our sky-fitting procedure, while the lower line shows that produced by a normal two-dimensional function fitting. The lines are shifted down by 110 ADU and 150 ADU, respectively, for ease of display. One can compare them and easily find that our procedure produces smaller residuals. The arrows in panels 2, 3, and 4 show the positions where the slices cross the ring.

the sources of random errors, this implies an intrinsic accuracy of 20 ADU pixel^{-1} for the faintest signal in the 6660 Å image and 19 ADU pixel^{-1} in the 8020 Å image *where we can explicitly fit the sky*. Expressed in terms of surface brightness units, these errors correspond to a surface brightness of 29.4 mag arcsec^{-2} in the 6660 Å image, and 27.7 mag arcsec^{-2} in the 8020 Å image. In masked regions, this intrinsic error will be larger and more systematic because of the residual surface brightness around the masks of bright stars.

Residual foreground star subtraction.—The slight imperfections in the star-masking process can be estimated from the slices given in Figures 7 and 8. By examining the regions around the brighter subtracted stars, it is apparent that residual starlight affects our image at the level of 20–50 ADU pixel^{-1} in certain places around most of the brighter stars. From information given above, this occurs at surface brightnesses around the 29 mag arcsec^{-2} level in the 6660 Å combined image. It is also evident from Figures 7 and 8 that trying to mask the stars to fainter light levels would indeed remove all but a very few of the remaining pixels in these cuts. The complications in our analysis of these data introduced by this compromise are discussed below.

Table 4 summarizes the sources of variation in our surface photometry in 6660 Å that are generally present in our 6660 Å combined image. This example assumes that the observed surface brightness gives us 50 ADU counts from the galaxy, 37,066 from the sky with a bin size of 45 × 45 pixels. We choose this bin because it is the farthest measured point from the galaxy midplane in our perpendicular profiles. It can be shown that the irreducible systematic error in determining sky background combined with unavoidably imperfect star masking determines the ultimate limit of the accuracy that can be achieved.

In reality, we must add to this value (24 ADU) the more problematic residuals that we see around bright stars within

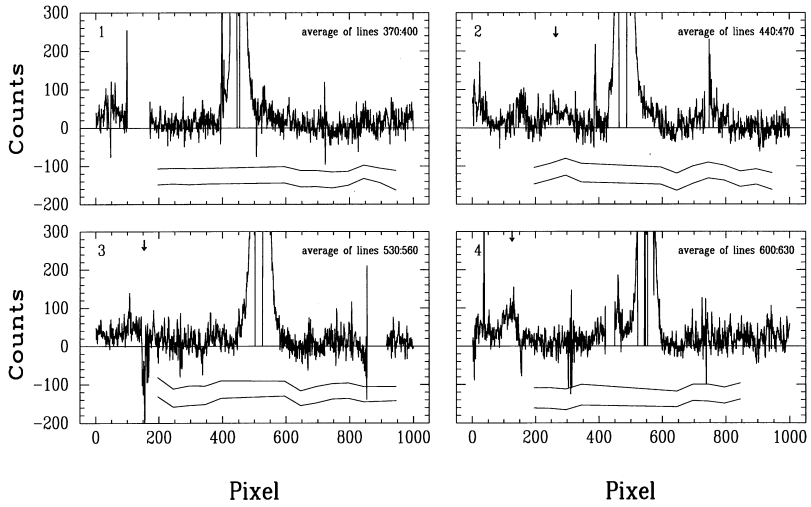

FIG. 8.—Same as Fig. 7, but for slices in the background-subtracted 8020 Å image

TABLE 4

SUMMARY OF LIMITING ERROR SOURCES IN A 45 × 45 PIXEL BIN IN THE 6660 Å IMAGE

Source of Variation	ADU	%
Reducible noise:		
Readout noise	0.6	0.002
Photon statistics	2.1	0.006
Bias and dark	0.02	0.00005
Flat-fielding errors	0.08	0.0002
Surface brightness fluctuations	0.3	0.0008
Irreducible noise:		
Large-scale FF errors	3.7	0.01
Systematic error of background subtraction	18.0	0.05
Total	23.9	0.06

the masked region around the galaxy and ring. At its lowest level ($\sim$20 ADU), the error is comparable to our minimum error; at its highest ($\sim$50 ADU), it dominates the minimum error. As we will see, residual surface brightness from bright stars probably imposes the ultimate limit on our investigation of the halo of NGC 5907.

3. SURFACE BRIGHTNESS DISTRIBUTION OF, AND NEAR, NGC 5907

3.1. *Color and Magnitude of NGC 5907*

We measure the total magnitude of NGC 5907 to a surface brightness of 27 mag arcsec^{-2} of $m_{6660} = 9.9 \pm 0.02$ and $m_{8020} = 9.5 \pm 0.02$. To obtain these values we replaced the areas excluded because of foreground stars with the mean value of the surrounding background. Expressing the same point in more standard terms, we use the fact that we find an average transformation of $R-I = m_{6660} - m_{8020} - 0.2$ mag, based on comparison with existing surface photometry of NGC 5907 (§ 4.2). Thus, our observations indicate that NGC 5907 itself has $R-I = 0.2 \pm 0.04$. If we exclude a rectangle around the obvious dust lane in this galaxy, we find the average $R-I$ color to be -0.1 ± 0.1. This bluer color refers to the average value for stars less affected by dust in the disk, and it is typical for a stellar population dominated by younger stars.

3.2. *Edge-on Stellar Warp*

The H I warp of NGC 5907, first found by Sancisi (1976), is strongly confirmed by our own VLA 21 cm H I observations (Shang et al. 1998). Given the warp in the H I gas, it is logical to search for an analogous warp in the stars. While van der Kruit (1979) only had marginal evidence for such a stellar warp, Sasaki (1987) claimed to detect an optical warp at a projected radial distance along the major axis from 13.3 kpc to 24.0 kpc from the center of the NGC 5907. It has been shown that there are similarities between the optical warp of Sasaki and the H I warp (R. Sancisi 1993, private communication). Figure 7 of MBH gives evidence of the start of a stellar warp at 4.1 kpc from the center of the galaxy.

The warp in each of our combined images is determined by measuring the horizontal distances between the surface brightness profiles of two sides of the galaxy around a fiducial position angle and then measuring their mean offset as a function of distance along the galaxy's major axis. Figure 9 shows the optical stellar warps calculated from our brightness profiles parallel to the minor axis. We find a warp in the galaxy that begins near the center of the galaxy (at 4.1 kpc, in agreement with what MBH found) and changes continuously outward to at least 16 kpc from the center, such that at a radius of 16 kpc, the warp deviates about 0.4 kpc ($\sim$4 pixels) above the average galaxy plane. We see the same warp in both our 6660 Å image and in our 8020 Å image.

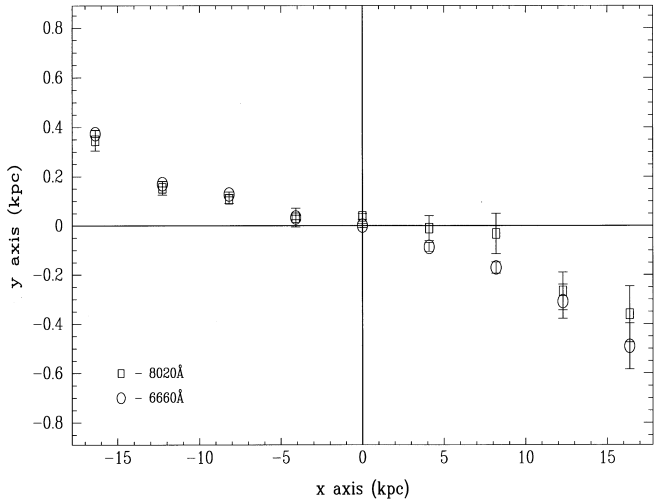

FIG. 9.—Stellar warp of NGC 5907 measured in two bands. The circles are from a 6660 Å image and the squares are from a 8020 Å image. The x-axis is along the galaxy plane, which is determined by fitting the symmetry axis of the galaxy. The stellar warp is obvious even in the cut nearest the galaxy center.

In regard to investigations of faint surface brightness far from the midplane of an edge-on galaxy, warps are likely to occur with greater frequency along the line of sight to the disk than at the disk edges, given relative angular coverage. A galactic disk showing a warp at its edges increases the possibility that the galaxy is also warped along the line of sight. This face-on warp may distort galactic surface brightnesses at large z-distances from the galaxy plane in a nonaxisymmetric way, as opposed to the expected symmetry of a halo. As such, separating the two kinds of possible sources of high z surface brightness is possible in principle. In the case of NGC 5907, we note some indications in our current VLA observations that the H I layer is higher near the center of the galaxy than outside the center (Shang et al. 1998). We explore the consequences of this hypothesis below.

3.3. *Stellar Ring*

As shown in Shang et al. (1998) and as is evident from the deep images we present here (Figs. 6*a* and 6*b*), NGC 5907 is surrounded by a faint, luminous ring. Our schematic for this ring is shown in the inset in Figure 6*a*. As discussed in Shang et al. (1998), the ring is reasonably elliptical in shape and of a similar angular size to the galaxy itself, with the center of NGC 5907 near one focus of the ellipse. The reality of this ring has been confirmed on other CCD images (see Shang et al. 1998), and part of the ring can be faintly seen in Figure 3 of MBH (although they do not recognize it as part of a ring). Various arguments concerning the origin of this ring are advanced in Shang et al. (1998), from which we conclude that by far the most likely interpretation involves a dwarf spheroidal galaxy in the process of being torn apart by a strong tidal encounter with NGC 5907.

The physical particulars of the ring indicate that the luminosity distribution within it is irregular both in surface brightness and in apparent thickness. The maximum width of the ring is found at the northeast end of its major axis (40 pixels = 68″.4 = 3.6 kpc at the distance of NGC 5907), while its narrowest width is found near the region where the ring overlaps NGC 5907 (20 pixels = 34″.2 = 1.8 kpc). In our estimate of the total brightness of the ring, we are limited by masked areas within NGC 5907 itself, which obscure the part of the ring nearest the galaxy. This means that the only unambiguous measurements we can make are of the ring's unmasked pixels in the clearer northeast half. We find the average surface brightness in the northeast half of the ring to be 28.0 ± 0.3 mag arcsec^{-2} in the 6660 Å image and 28.3 ± 1.8 mag arcsec^{-2} in the 8020 Å image. The much larger error for the ring surface brightness at 8020 Å is expected, given our error budget estimate (§ 2.8). If we assume that the whole ring has this average surface brightness, we obtain total magnitudes of $m_{6660} = 14.7 \pm 0.3$ and $m_{8020} = 15.0 \pm 1.8$ for the ring. These estimates, however, may merely put limits on the brightness or faintness of the ring; it is not obvious how irregular the distribution of light may be in those regions we cannot investigate, because they overlap with the galaxy and with foreground stars.

The larger error on m_{8020} precludes quoting a reasonable color for the ring as a whole. If we measure just the highest surface brightness features in the ring (denoted by arrows in Fig. 8 and 9), we find 26.8 ± 0.1 mag arcsec^{-2} in 6660 Å and 26.1 ± 0.2 mag arcsec^{-2} in 8020 Å, yielding a color index $m_{6660} - m_{8020} = 0.7 \pm 0.3$ (or $R-I = 0.5 \pm 0.3$). To confirm this result, we also measure the total flux in the brightest area of the ring by (indicated by the parallelogram in Fig. 6*a*), yielding an average surface brightness of 27.0 ± 0.1 mag arcsec^{-2} in 6660 Å and 26.4 ± 0.3 mag arcsec^{-2} in 8020 Å, implying an $R-I$ color of 0.4 ± 0.4. Measuring the second brightest area of the ring yields a similar result. On average, we measure the ring to have an $R-I$ color of 0.5 ± 0.3, consistent with the $R-I$ colors for Galactic globular clusters of metallicities [Fe/H] ~ -1.0 (see Peterson et al. 1993).

3.4. *Cuts Perpendicular to the Disk*

In Figure 6*a*, we show how the perpendicular cuts used by MBH are related to our combined 6660 Å image. (Rather than term these cuts "along the minor axis," we prefer to designate them as cuts "perpendicular to the major axis.") Like MBH, we designate each cut by a letter and number, with "A" indicating the central cut, "B1" and "B2" the cuts nearest the center (B1 to the northeast and B2 to the southwest), and "D1" and "D2" the cuts in the outer parts of the galaxy.

To increase S/N along these cuts, we bin 45 pixels in width. To keep S/N approximately constant with increasing z-distance from the galaxy midplane, we increase the heights of the bins exponentially with increasing z-distance, with 1 pixel the smallest height and 59 pixels being the largest. This procedure is directly analogous to the one employed by MBH. For our estimate of the galaxy's surface brightness, we take the mode of each bin sampled. The reason for this is that undetected background sources, as well as residuals from the star-masking procedure, will tend to bias upward the mean and median ADU counts tabulated in each bin. We experimented with alternate definitions of the flux in a bin and found that, while the problem can be partially resolved by σ clipping algorithms, the best solution is to use mode value instead of the mean or median. A σ clipping algorithm is used to eliminate bad pixel values from the histograms (of which a few still remain in the combined image).

The perpendicular profiles we derive from the 6660 Å image are given in Figures 10 and 11 from the 8020 Å image, and they are tabulated in Table 5 both for completeness and to assist future studies of this galaxy by others. The profiles of the two sides (northeast and southwest) about the

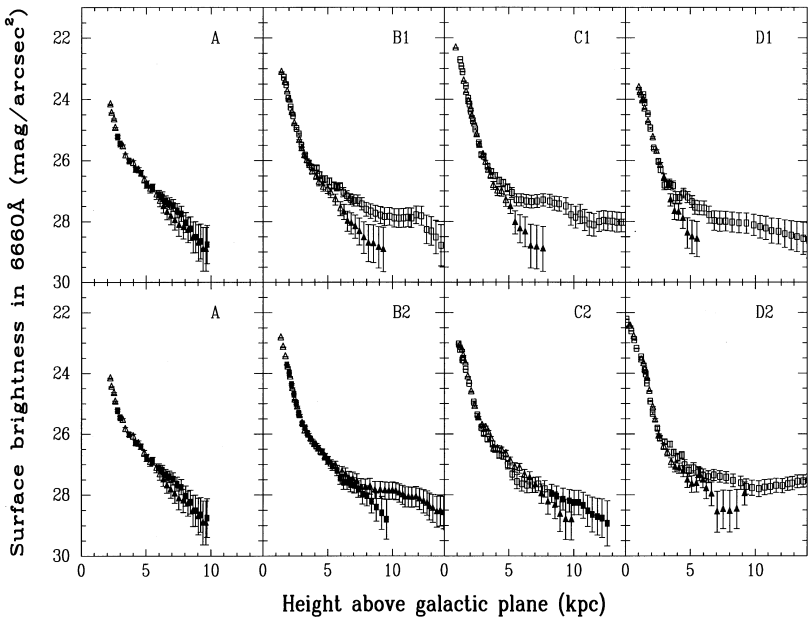

FIG. 10.—Surface brightness profiles in the 6660 Å passband for the seven MBH-consistent cuts perpendicular to the galaxy plane. Each panel corresponds to one of the cut shown in Fig. 6*a*, and the separate measurements of the two sides of the galaxy plane are shown. The data of the northeast and soutwest side of the galaxy plane are denoted by squares and triangles, respectively. The open symbols denote the points affected by the ring. Central regions of the galaxy are excluded because of star and dust masking. The asymmetries at faint surface brightnesses in these cuts are discussed in the text.

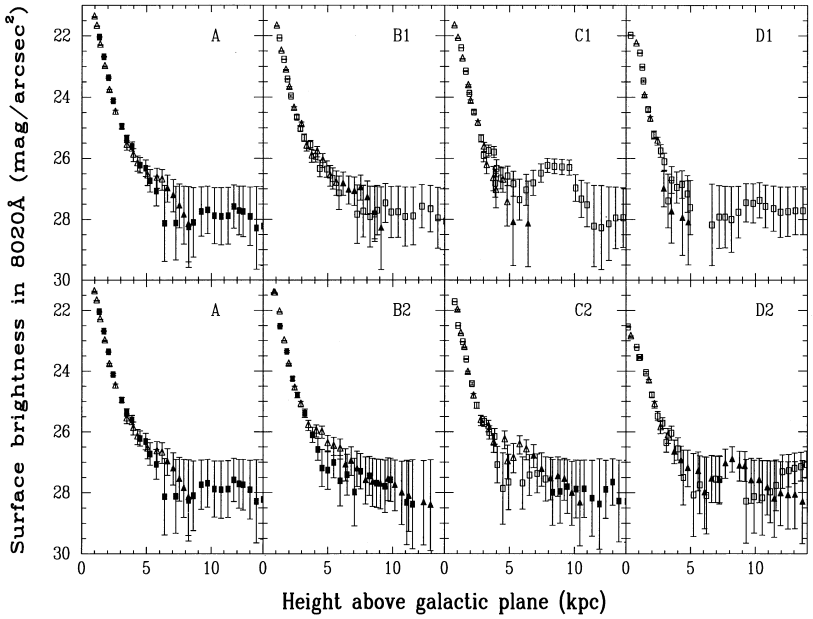

FIG. 11.—Same as Fig. 10, but for 8020 Å

galaxy plane are folded around the curved warp line to remove the effect of the edge-on warp. Those parts of the profiles fainter than $m_{6660} = 29$ and $m_{8020} = 28$ (about 0.1% of sky) are not presented, as our limiting systematic errors make fainter surface brightnesses uncertain by more than 1 mag. In our plots of these perpendicular profiles, filled symbols represent parts of the profile *not* influenced by the surface brightness distribution in the ring (Shang et al. 1998), while open symbols indicate the parts of profiles in which light from the ring, as well as a possible warp in front of the galaxy, affects what we see.

It is obvious that at large z-distances from the plane of the galaxy, the faint surface brightness distribution in the 6660 Å image around NGC 5907 *is not symmetric about the midplane of the galaxy*. Only in the case of the A and C2 cuts are the profiles on the northeast and southwest sides of the galaxy consistent within the errors at faint surface brightnesses. The northeast sides of the profiles in cuts C1, D1, and D2 are systematically brighter than the southwest sides in these cuts. In the case of cuts B1 and B2, one side is brighter than the other, but the sense of asymmetry changes from B1 to B2. The B1 profile (to the northwest of the galaxy center) has its northeast side significantly brighter than its southwest side. In contrast, the B2 profile (to the southwest of the galaxy center) has its southwest side brighter than its northeast side, opposite to the symmetry seen in the B1 profile. Larger errors at faint levels in our 8020 Å image preclude any comparable conclusions being made for the cuts in that image.

Based on what we see in our 6660 Å image, therefore, we find that the faint surface brightness distribution around NGC 5907 is asymmetric. With these data, we can confidently rule out the presence of a halo in this galaxy beyond a distance of 5 kpc.

3.5. *Ring, Foreground Stars, and Possible Warp Influences on the Asymmetry of the Perpendicular Profiles*

As can be seen by comparing the perpendicular profiles in Figures 10 and 11 with the positions of the cuts relative to the ring in Figure 6*a*, cuts C1, D1, and D2 all intersect the ring on the northeast side of the galaxy. The effect of confusion with the ring on the perpendicular profile is also shown

TABLE 5

PERPENDICULAR SURFACE BRIGHTNESS PROFILES OF NGC 5907 IN THE 6660 AND 8020 Å IMAGES

Distance (arcsec)	Distance (kpc)	6660 Å (mag arcsec^{-1})	Error (6660 Å) (mag arcsec^{-1})	8020 Å (mag arcsec^{-1})	Error (8020 Å) (mag arcsec^{-1})
Cut A, $r = 0$ kpc:					
−184.63[a].....	−9.83	28.91	0.72	...	...
−180.35[a].....	−9.60	28.91	0.72	...	...
−173.43[a].....	−9.23	28.70	0.60	...	...
−165.56[a].....	−8.81	28.52	0.51	...	...
−158.21[a].....	−8.42	28.28	0.41	...	...
−151.28[a].....	−8.05	28.19	0.38	27.81	0.91
−144.70[a].....	−7.70	28.12	0.36	27.54	0.71
−138.54[a].....	−7.37	27.96	0.31	27.24	0.54
−132.64[a].....	−7.06	27.82	0.28	27.24	0.55

NOTE.—Table 5 is presented in its entirety in the electronic edition of the Astronomical Journal. A portion is shown here for guidance regarding its form and content.

[a] Data affected by foreground star contamination and a possible line-of-sight warp.

[b] Data affected by the ring.

in Figure 7 (*panel 1*; the apparently smooth gradient in the outer profile of the galaxy, from pixel numbers 600 to 750, is due almost entirely to the presence of the ring in this region; see Fig. 6*a*).

If we take the average surface brightness of the ring (28 mag arcsec^{-2} in the 6660 Å image; see § 3.3) as a conservative estimate of the ring's surface brightness near the galaxy, most of the faint extensions seen in cuts C1, D1, and D2 on the northeast side of the galaxy can be attributed to ring light. Because we are able on separate grounds to make a prima facie case that the ring is elliptical in shape, with the center of NGC 5907 at one of its foci (see Shang et al. 1998), it is difficult to disentangle true galaxy light from possible ring light in the A cut on the southwest side of the galaxy at surface brightnesses fainter than 28 mag arcsec^{-2} in the 6660 Å image.

Of the remaining three of the six noncentered cuts (B, C, and D) made, C2 has the least foreground star contamination, although there remains some star contamination on its southwest side. In contrast, both B1 and B2 include large sections of the masks around bright stars: B2 on its southwest side, B1 on its northeast side, and similarly for C1 on its northeast side, D1 on its northeast side, and D2 on its southwest side. Interestingly, in every case, the side of the galaxy that is brighter is contaminated more by foreground stars than its partner. This would strongly suggest that residual starlight at low light levels (6660 Å surface brightnesses of 29 mag arcsec^{-2} and fainter) is contributing to the differential effect seen in these cuts at 6660 Å surface brightnesses of 28 mag arcsec^{-2} and fainter.

On the other hand, *if* this galaxy has a face-on warp, one might expect that the warp would give an asymmetric distribution perpendicular to the center of the disk near the galaxy center, i.e., in cut B1 as opposed to cut B2. While such an effect is certainly seen, the apparently irreducible effects of foreground star contamination make it highly unlikely that we will be able to unambiguously detect a face-on warp in this galaxy, even if it exists. NGC 5907 simply has too many foreground stars around it to be a good edge-on galaxy candidate in which to find a face-on warp.

4. COMPARISON WITH PREVIOUS RESULTS

4.1. *Comparison with Results of MBH*

To facilitate a close one-to-one comparison with the published results of MBH, H. Morrison kindly sent us unpublished surface brightnesses used to construct their perpendicular cut diagrams in the MBH paper. If we compare the broadband *R* surface brightness profiles from MBH given in Table 6 with our own 6660 Å surface brightness profiles given in Table 5, it is apparent that, for similar errors, our data go approximately 1.5 mag fainter than those of MBH. The main reason is that the sky is much fainter in our intermediate-band filter, which avoids the brightest night-sky lines, than it is in the broadband *R* filter used by MBH (0.6 e^- s^{-1} arcsec^{-2} in our combined 6660 Å image as opposed to the 7.4 e^- s^{-1} arcsec^{-2} quoted by MBH for their *R*-band data).

As is evident from the graph presented in Sackett et al. (1994), these authors combined the northeast and southwest sides of each cut to form one combined perpendicular profile per cut. With our higher accuracy at fainter light levels, we are able to see the asymmetry in the faint light distribution perpendicular to the disk that MBH and Sackett et al. could not.

We compare the perpendicular profiles of MBH with our 6660 Å image profiles in Figure 12. A zero point of 0.3 is added to the *R*-band data of MBH to bring the two filter systems onto the same photometric system at bright levels of the galaxy. While we note that MBH cite results only for *R*-band surface brightnesses brighter than 27 mag arcsec^{-2},

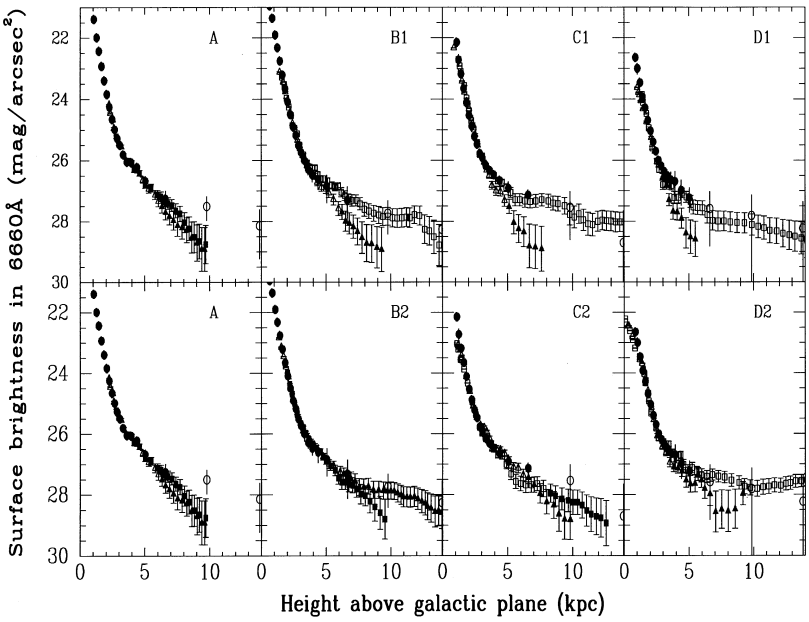

FIG. 12.—Comparison of our 6660 Å data with those of MBH, with a zero-point shift of 0.3 mag applied to the MBH data to account for the different passbands used. The circles are the data of MBH that were sent to us by H. Morrison, which go to fainter surface brightnesses than those used by MBH in their actual paper. The filled circles are the reliable data claimed by them and used by Sackett et al. (1994), while the open circles (fainter than 27 mag arcsec^{-2}) were not used in those papers. The other symbols have the same meaning as in Fig. 10. Note the generally good agreement between our data and those of MBH (save for cuts A and C2) even at surface brightnesses fainter than 27 mag arcsec^{-2}.

TABLE 6

MBH Surface Brightness Profiles of NGC 5907 in *R* Band

Distance (arcsec)	Distance (kpc)	*R* (mag arcsec^{-1})	High Error (mag arcsec^{-1})	Low Error (mag arcsec^{-1})
Cut A, $r = 0$ kpc:				
11.55	0.61	19.99	0.00	0.00
15.79	0.84	20.51	0.00	0.00
19.69	1.05	21.08	0.00	0.00
23.81	1.27	21.69	0.00	0.00
27.00	1.44	22.13	0.00	0.00
30.82	1.64	22.62	0.01	0.01
34.65	1.84	23.09	0.01	0.01
38.46	2.05	23.53	0.01	0.01
42.25	2.25	23.95	0.02	0.02
46.19	2.46	24.35	0.03	0.03
50.02	2.66	24.69	0.04	0.04
53.90	2.87	24.98	0.05	0.06
57.76	3.08	25.20	0.06	0.07
62.30	3.32	25.50	0.11	0.13
67.73	3.61	25.74	0.14	0.16
74.04	3.94	25.76	0.10	0.11
82.59	4.40	25.92	0.11	0.13
94.78	5.05	26.37	0.17	0.20
123.88.....	6.60	26.95	0.27	0.36
183.67.....	9.78	27.20	0.33	0.47
260.55.....	13.87	27.84	0.53	1.10
334.53.....	17.81	28.00	0.60	1.44
410.94.....	21.88	28.28	0.73	3.36
466.15.....	24.82	33.40	4.33	0.00
Cut B, $r = 4.1$ kpc:				
5.78	0.31	19.92	0.00	0.00
8.23	0.44	20.11	0.00	0.00
12.19	0.65	20.65	0.00	0.00
15.97	0.85	21.05	0.00	0.00
20.31	1.08	21.60	0.07	0.07
23.49	1.25	22.02	0.03	0.03
27.09	1.44	22.46	0.05	0.05
30.80	1.64	22.91	0.04	0.04
34.65	1.84	23.36	0.06	0.06
38.51	2.05	23.79	0.11	0.12
42.38	2.26	24.20	0.12	0.14
46.17	2.46	24.60	0.13	0.14
50.05	2.67	24.87	0.14	0.16
53.94	2.87	25.21	0.14	0.16
57.74	3.07	25.43	0.18	0.21
62.26	3.32	25.69	0.21	0.26
67.82	3.61	25.98	0.17	0.20
73.92	3.94	26.17	0.19	0.24
82.27	4.38	26.30	0.27	0.35
94.99	5.06	26.54	0.37	0.56
125.02.....	6.66	27.01	0.46	0.83
183.68.....	9.78	27.43	0.42	0.70
262.36.....	13.97	27.96	0.72	3.17
333.43.....	17.75	27.88	0.59	1.37
415.87.....	22.14	28.57	0.73	3.30
466.49.....	24.84	33.40	5.15	0.00
Cut C, $r = 8.2$ kpc:				
20.82	1.11	21.84	0.01	0.01
23.55	1.25	22.42	0.19	0.23
26.97	1.44	22.88	0.14	0.17
30.81	1.64	23.35	0.11	0.12
34.66	1.85	23.81	0.07	0.08
38.55	2.05	24.23	0.08	0.09
42.34	2.25	24.58	0.12	0.13
46.21	2.46	24.92	0.15	0.17
50.04	2.66	25.17	0.13	0.15
53.92	2.87	25.47	0.13	0.15
57.74	3.07	25.62	0.16	0.19
62.32	3.32	25.85	0.15	0.17

TABLE 6—*Continued*

Distance (arcsec)	Distance (kpc)	R (mag arcsec^{-1})	High Error (mag arcsec^{-1})	Low Error (mag arcsec^{-1})
67.74	3.61	26.02	0.09	0.10
73.93	3.94	26.17	0.10	0.12
82.39	4.39	26.36	0.15	0.18
94.98	5.06	26.61	0.22	0.27
123.47.....	6.57	26.83	0.18	0.21
184.48.....	9.82	27.24	0.53	1.07
261.75.....	13.94	28.40	1.05	5.00
331.70.....	17.66	27.92	0.78	5.48
413.16.....	22.00	27.96	0.78	5.44
462.21.....	24.61	28.05	0.66	1.98
Cut D, $r = 12.3$ kpc:				
16.56	0.88	22.34	0.11	0.12
19.49	1.04	22.70	0.17	0.21
23.33	1.24	23.16	0.09	0.10
26.98	1.44	23.62	0.07	0.07
30.84	1.64	23.98	0.06	0.06
34.63	1.84	24.39	0.03	0.03
38.54	2.05	24.73	0.09	0.10
42.38	2.26	25.09	0.08	0.08
46.24	2.46	25.40	0.12	0.14
49.95	2.66	25.69	0.09	0.09
53.92	2.87	25.88	0.21	0.25
57.74	3.07	26.04	0.25	0.33
62.52	3.33	26.19	0.20	0.24
67.78	3.61	26.33	0.25	0.32
73.85	3.93	26.39	0.34	0.49
82.73	4.41	26.68	0.34	0.51
94.64	5.04	26.93	0.34	0.49
124.14.....	6.61	27.28	0.57	1.25
185.07.....	9.85	27.51	0.69	2.31
259.71.....	13.83	27.93	0.87	5.47
337.33.....	17.96	27.75	0.89	5.65
403.18.....	21.47	27.80	0.87	5.60
469.57.....	25.00	28.40	0.96	5.00

the actual data given to us by H. Morrison go fainter than this. As neither MBH nor Sackett et al. (1994) give actual surface brightness profile information, we choose to base our comparison on the data sent to us by H. Morrison.

We find generally good agreement with the MBH data in most cases, even at low light levels. Good agreement is found between our data and those of MBH, both in form and zero point, for distances less than 5 kpc from the galaxy midplane in all cuts. This strongly supports the accuracy of the zero points obtained by both MBH and us and shows that our perpendicular profiles are similar, typically at surface brightnesses brighter than 27 mag arcsec^{-2}.

Above a distance of 5 kpc from the galaxy midplane, the comparison must take into account the asymmetry of the faint light distribution seen. Namely, for the cuts B1, B2, C1, D1, and D2, the two faintest measurements of MBH are probably measuring only the brighter flux from one side of the galaxy (otherwise, because of the asymmetry, we should find the MBH data to be 0.75 mag fainter than ours). This conclusion is consistent with what we see in Figure 12, in which the faintest MBH measurements are in accord with our higher levels of surface brightnesses measured on one side of the galaxy or the other. The two exceptions to this agreement at low light levels are the A and C2 cuts, where the surface brightness difference systematically occurs at levels of 27.5 mag arcsec^{-2} and fainter in these two cuts.

This comparison suggests strongly that in both the MBH data and our own, the surface brightness profiles are affected by residual foreground star subtraction at very low light levels. Inspection of MBH's Figure 3 and the figure modeled at a higher resolution in Sackett et al. (1994), show this to be the case. One can see extra flux around the brighter masked stars in a similar kind of asymmetric pattern as that seen in our own masked 6660 Å image (Fig. 6*a*). In addition, the two bright stars to the lower left of the galaxy in their image show CCD bleeding along the columns, which is not completely taken out by their masking procedure.

Thus, we conclude that our data, both in zero point and in form, are in good agreement with the data of MBH at low light levels. Observed differences are as likely to be attributable to issues concerning foreground star subtraction as to any other kind of systematic error. From this we conclude that the data used by MBH and Sackett et al. (1994) for their investigations into the possible thick disk and halo of NGC 5907 were as contaminated as ours by ring light and residual light from masked foreground stars.

4.2. *Comparison with Results of Lequeux et al. and Rudy et al.*

The J, K, V, R, and I surface brightness gradients in NGC 5907 are given in Rudy et al. (1997) for both their observations (J, K, and R) and those of Lequeux et al. (1996) (V and I). There are no published numbers for the

additional *B* observations by Lequeux et al. (1998). In comparing these data with our own, we first need to determine whether the surface photometry was deep enough to detect the ring around NGC 5907. In the case of MBH, the answer is yes (§ 4.1).

Of the observations by Rudy et al. (1997) and Lequeux et al. (1996), the evidence as to whether the Rudy et al. (1997) data did go faint enough to detect the ring in the near-IR is inconclusive. Rudy et al. do remark that their surface brightness profiles show an asymmetry, with the northeast side of the galaxy having more light at low levels than the southwest side. However, neither we nor MBH see this "bump" in our data. In the case of Lequeux et al. (1996), it is apparent both from the image and the surface brightness profiles they give that their observations did not go faint enough to detect the ring.

Figure 13 compares the perpendicular profiles along the minor axis of NGC 5907 in the 8020 Å image with that given by Lequeux et al. (1996) for the *I* band and by Rudy et al. (1997) for the *J* and *K* band. These data are given in Table 7, along with the Rudy et al. *R*-band data and the Lequeux et al. *V*-band data (for completeness). The zero-point shift in the *I* band is 0.1, implying a zero-point shift between $m_{6660}-m_{8020}$ and $R-I$ of about 0.2.

There is generally good agreement within the quoted errors among the *J*, *K*, and 8020 Å perpendicular profiles. The one exception is the presence of the above-mentioned bump on the northeast side of the Rudy et al. (1997) *J* and *K* data, which is not present in either our data, those of MBH (see Fig. 12, A cut), or Lequeux et al. (1996). This indicates that few detectable color gradients can be formed from these three passbands, although, if a significant color gradient does exist here, the mutual errors are large enough to hide it. The absence of quoted errors for the Lequeux et al. (1996) *I*-band data prevents us from making an accurate assessment of the extent to which our data agree with theirs. Even so, within the cited errors of the other data sets, the only differences we find between the Lequeux et al. (1996) *I*-band perpendicular profile and those of the other data sets are in the inner three points measured to the northeast.

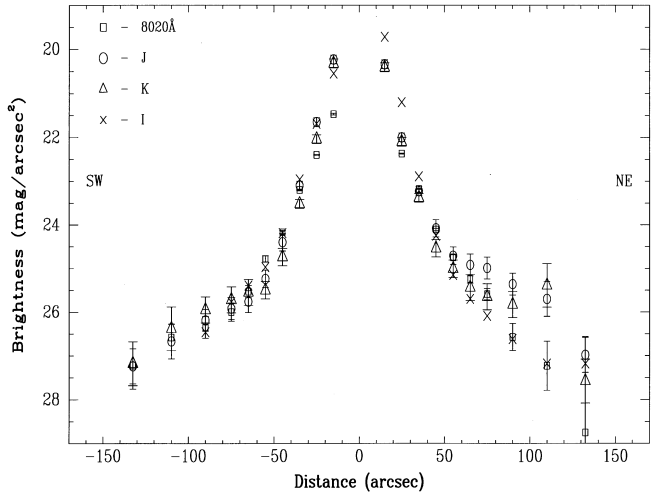

FIG. 13.—Comparison of our 8020 Å data with infrared data from Rudy et al. (1997; *J* and *K*) and Lequeux et al. (1996; *I*), with the zero point applied to the published data as discussed in the text. Note the generally good agreement among the different passbands, with their mutual errors, except for the bump seen in the data of Rudy et al. but not in the other data sets.

In contrast, the *J*, *K*, and 8020 Å data for these three measured points are in very good agreement. Once again, exactly how each group handled the problem of foreground star contamination probably leads to the differences seen in the inner part of the profile as shown in Figure 13.

4.3. *Colors of NGC 5907 Perpendicular to its Disk*

As is evident from this comparison with other data, it is very difficult to obtain reliable colors of galaxies at faint surface brightnesses. The errors of both passbands involved in forming the color combine quadratically, and the resulting color differences are often small relative to this error. As shown in Figure 14, this is clearly the case for the color gradients we are able to form from our data perpendicular to the disk of NGC 5907 in the $m_{6660}-m_{8020}$ color. The error bars are formal 1 σ errors per measurement.

TABLE 7

COMPARISONS WITH SURFACE BRIGHTNESS PROFILES FROM OTHER OBSERVERS

Position (arcsec)	6660 Å	8020 Å	*J*	K_s	*R*	*V*	*I*
−145 to −120.....	27.80	27.22	25.64	24.48	...	...	...
−120 to −100.....	27.15	26.58	25.07	23.68	26.72	...	...
−100 to −80	26.64	26.35	24.59	23.25	26.31	27.58	26.36
−80 to −70	26.28	26.00	24.32	23.02	25.96	27.00	25.67
−70 to −60	25.82	25.53	24.16	22.85	25.71	26.50	25.29
−60 to −50	25.31	24.78	23.64	22.80	25.02	25.95	24.87
−50 to −40	24.58	24.17	22.80	22.04	24.15	25.04	24.09
−40 to −30	24.09	23.20	21.50	20.82	23.04	23.85	22.86
−30 to −20	...	22.40	20.05	19.34	21.79	22.63	21.59
−20 to −10	...	21.47	18.63	17.62	20.56	21.65	20.45
10 to 20	...	...	18.74	17.71	20.56	20.92	19.62
20 to 30	...	22.37	20.40	19.40	21.79	22.41	21.10
30 to 40	...	23.18	21.63	20.68	23.04	23.77	22.79
40 to 50	24.71	24.11	22.48	21.84	24.15	25.06	24.15
50 to 60	25.52	24.75	23.11	22.31	25.02	26.04	25.05
60 to 70	25.91	25.24	23.32	22.74	25.71	26.68	25.60
70 to 80	26.19	25.59	23.39	22.95	25.96	27.15	25.99
80 to 100.....	26.61	26.57	23.76	23.13	26.31	27.67	26.52
100 to 120	27.06	27.23	24.10	22.69	26.72	28.30	27.08
120 to 145	27.60	...	25.38	24.88	...	...	27.08

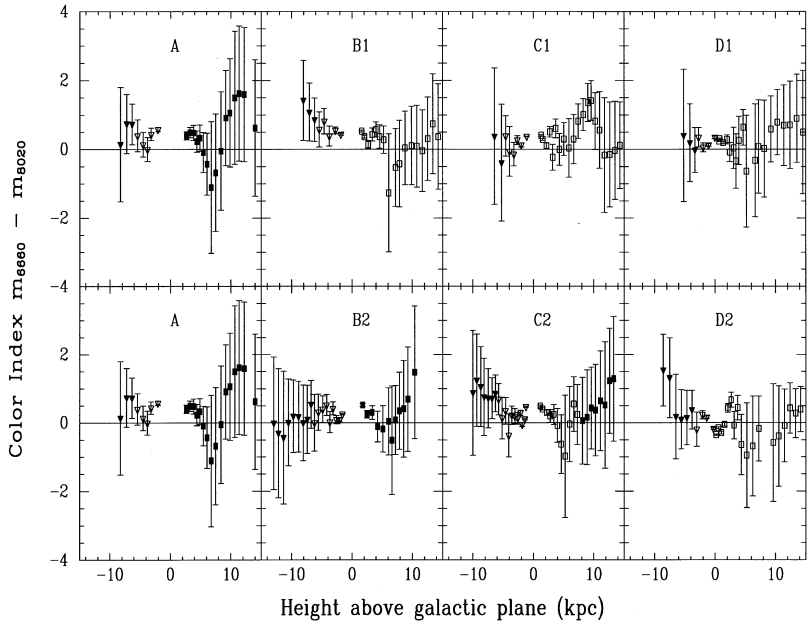

FIG. 14.—NGC 5907 $m_{6660}-m_{8020}$ color profiles. Measurable color gradients become bluer with distance from the galaxy midplane in all cuts except D2, where the color gradient actually becomes redder with distance from the midplane. Symbols are the same as in Fig. 10 and Fig. 11. It is apparent that the errors in the colors preclude any meaningful measurement of the color gradient outside of 4 kpc from the plane of this galaxy.

Because 2 σ to 3 σ errors are also likely to be present in these data, it is apparent that the color gradients 4 kpc and farther from the disk of NGC 5907 are completely dominated by observational error.

Interestingly enough, within 4 kpc of the galaxy plane, we find that the color gradients in many of the cuts become bluer in $m_{6660}-m_{8020}$ with increasing radius, with cut D2 being the notable exception. In D2 alone, the color gradient seems to get *redder* on both sides of the galaxy with distance from the midplane.

As can be seen also in Figure 13, colors formed outside the 4 kpc midplane region from any of the published passbands show little difference within the mutual errors of observations. The only exceptions in the published literature are the questionable northeast bump in J and K in the Rudy et al. data, and the J, K observations of James & Casali (1998). While James & Casali claim to detect significant J and K flux from NGC 5907 at high z-distance from the galaxy midplane, their data are likely as systematically affected by the galaxy ring (not mentioned in their paper) and bright star halos as all other such data for this galaxy.

4.4. *Limiting Factors in Faint Galaxy Surface Photometry*

We have already detailed the three sources of systematic error in faint galaxy surface photometry: (1) systematic errors in determining the flat field, (2) systematic errors in determining the sky background, and (3) residual surface brightness from bright stars that cannot be easily masked. Most observers try to take these factors into account (although not all explain in their papers that they are doing so; see Lequeux et al. 1996, 1998). However, there are two other sources of zero-point errors in sky-level determination that are not discussed in the previous papers. We include these now to complete our discussion of the data.

First is the fact discussed above that CCDs have wavelength-dependent QEs and that this dependence differs slightly from pixel to pixel. Galaxies and the sky background can have very different colors, depending on which part of the spectrum is observed, how bright the night-sky lines are, how bright the sky continuum is, etc. If the difference in color is large enough, the effective wavelength of a filter can be changed sufficiently to influence its QE in a detectable manner, and the sky level estimated will be affected in direct proportion to the percent change in QE. Take the R-band observation as an example. Because the galaxy effective wavelength could be off by 50–100 Å from the sky effective wavelength in the broadband R, it is entirely possible that the QE of the CCD could differ by one part in 1000, from the galaxy effective wavelength to the sky effective wavelength. The zero point of the B, V, and I observations are similarly affected.

The issue for J and K observations is somewhat different, because here the sky level is so bright that it takes a triumph of instrumentation to get a good estimate of sky down to less than 0.01% accuracy. Again, however, if the IR array QE is a function of effective wavelength, accuracy in estimating the sky background in the broadband J and K filters will be limited by the difference in QE between galaxy color and sky color.

We chose intermediate-band filters for the BATC survey for several reasons, but one of the chief ones was to limit the bandpass sufficiently to prevent the differences in color of the objects observed from producing significant differences in the effective wavelength of the filters. In the case of the 6660 Å and 8020 Å filters, we designed them to avoid the brightest (and most variable) night-sky lines. As such, we believe the change in QE between galaxy and sky in our filters is much less than in the broadband filters. An additional advantage, of course, lies in the concomitantly much lower sky background (12 times lower in the 6660 Å filter than MBH obtained at KPNO in the broadband R).

The second source of nonmodeled zero-point error is the photometricity of the telescope field of view and the inherent nonflatness of the night sky. All telescopes suffer from

optical imperfections, most of which affect the transmission of light from the sky as a function of distance from the center of the field. It is primarily for this reason that the flatness of the night sky has become the final arbiter of how well the CCD image has been calibrated. Yet, the night sky itself is not flat, as Wild (1997) has pointed out. In our degree-sized BATC CCD fields, we clearly see the gradient of the night sky getting brighter toward lower altitudes. With CCD arrays becoming degree-sized and larger, this problem is only enhanced. While one takes many separate sky images at different times of night—so the altitudinal gradients go in different directions on the CCD—in the end the cancellation of the gradients cannot be perfect. Any residual gradient in the sky will then be mistaken as a gradient in the sensitivity of the CCD itself, and mistakenly divided out. It should be subtracted out of the image, as we have attempted to do in the present paper.

One advantage of using a Schmidt telescope for the BATC survey is that we position the CCD in the center 1° of a focal plane that has been specifically optimized to give as flat a field of view as possible in the center of a circle 3° in radius. This is true for any Schmidt telescope, which is one reason they are noted for giving the most reliable sky background estimates of any type of telescope.

The bottom line is that all sources of error conspire, such that it is extremely difficult to obtain sky background estimates and large-scale uniformities at accuracies better than 0.1% of the sky level. In defense of our results, we can point to much lower sky level and narrower passbands.

4.5. *Does NGC 5907 Have a Halo?*

Two facts are clear from the above analysis: (1) Our data substantially agree with the data in the literature for the surface brightness distribution seen perpendicular to the disk of NGC 5907. (2) We find the light distribution perpendicular to the disk of NGC 5907 to be highly *asymmetric* about the galaxy midplane, with one side enhanced relative to the other in each of MBH's B, C, and D cuts.

The difference between the present data set and those previously published is a combination of the advantage of using the center field of a Schmidt telescope and our use of intermediate-band filters. The use of the intermediate-band filters resulted in a much fainter sky; the large field of view of the Schmidt permitted features such as the ring to be easily identified. The large angular pixel size of our CCD ($1\farcs71$ pixel^{-1}) is an advantage when searching for faint surface brightness, as we minimize the number of pixels per large surface area.

Since we measure the ring around NGC 5907 to have an average 6660 Å surface brightness of 28 mag arcsec^{-2}, one can see from the images themselves (see Figs. 2*a* and 6*a*) that NGC 5907 does not have a halo at these faint surface brightnesses. This fact is more clearly evident on the southwest side of the galaxy, the side away from the bulk of the ring.

We are forced to the conclusion that asymmetries in foreground star PSFs lead to extra light around star masks, which combines with ring surface brightness to produce what faint extensions of surface brightness we see in the MBH cuts. This is because the asymmetries in the surface brightnesses derived from our images in the MBH cuts correlate with the degree of foreground star contamination in four of the six noncentered cuts. Overlap with the ring similarly contributes to the asymmetries seen in the other two of the noncentered cuts. Because we can see similar effects in the star-masked image of MBH (their Fig. 2) and because their data are in accord with ours, we are equally forced to the conclusion that their detection of a halo around NGC 5907 was an artifact caused by the same combination of ring light and unaccounted faint wings from their foreground stars that affects our data.

5. CONCLUSION

We have obtained very deep images of the edge-on galaxy NGC 5907 with two intermediate-band filters on the BATC system (see Fan et al. 1996), m_{6660} and m_{8020}. Via a detailed assessment of the sources of our errors, we show that our limiting magnitudes (where the observational error reaches 1 mag arcsec^{-2}) are 29.0 mag arcsec^{-2} in the 6660 Å image (corresponding to 28.7 in *R*-band measures) and 28.0 mag arcsec^{-2} in the 8020 Å image (close to the *I*-band system). This is over 1 mag fainter than previously published measurements, owing mostly to the much darker sky as seen in our intermediate-band filters.

We use a new method of sky subtraction that both can account for most of the foreground star contamination (by PSF-fitting the star profiles first, then subtracting the fit) and permits reasonable interpolation of sky under the galaxy region while also fitting the inherent lumpiness of the sky at low surface brightnesses (using interactive fits of bidirectional, low-order Legendre polynomials and heavy smoothing). Our use of diffuser-smoothed dome flats, already shown to give accurate photometric results over a wide range of stellar colors (Fan et al. 1996) are again shown to give reliable flat fields with these data. This is critical, as it can be easily shown (see Wild 1997) that the sky is not flat anywhere on degree-size scales.

As first shown by Shang et al. (1998), we detail the evidence that NGC 5907 has an elliptical-shaped ring of emission around it, which mostly likely is the remnant of a dwarf spheroidal galaxy that has been tidally torn apart. Within errors of 0.3–0.4 mag arcsec^{-2}, we show that the $R-I$ colors of the brighter part of this ring are consistent with the light coming from a moderately metal-poor old stellar population.

We investigate the surface brightness distribution perpendicular to the disk of NGC 5907 by taking the same cuts through the galaxy as MBH. We show that all of the faint, extended surface brightness we observe perpendicular to the disk of NGC 5907 (and above an altitude of 5 kpc) is most likely the result of contamination by ring light and by residual effects from foreground star contamination. The possibility of a face-on warp existing in NGC 5907, suggested by our H I observations, is too confused with foreground star contamination to permit us to prove or disprove its optical existence.

Our comparisons with the existing perpendicular profiles in the literature for NGC 5907 find us in substantial agreement with these data, once predicted zero-point differences are removed. Of particular note is that with the known zero-point difference between our 6660 Å filter and the *R* band removed, our data and those of MBH are in excellent agreement.

As such, we find that previous claims by Sackett et al. and others that NGC 5907 has a faint halo to be an artifact resulting from a combination of two factors. One is the added light complications from the presence of a previously unknown ring around the galaxy. The second factor is the

unaccounted residual effects of the foreground star masking procedures for both our data and those of MBH at faint levels. The lack of a halo around NGC 5907 is evident directly from our deep images of this galaxy (Figs. 2*a* and 6*a*), once one understands that the ring we detect has an average 6660 Å surface brightness of 28 mag arcsec^{-2}.

We thank Jinyao Hu and Xiaowei Liu for comments and discussions, Elias Brinks for his help in obtaining the VLA data, Heather Morrison for supplying us with the data of MBH, and the referee for helpful comments. The research done with the BATC Survey is supported by the Chinese Academy of Sciences, the Chinese National Natural Science Foundation, and the Chinese State Committee of Sciences and Technology. It is also supported in part by the National Science Foundation (NSF grant INT-93-01805), by Arizona State University, the University of Arizona, and Western Connecticut State University.

REFERENCES

Barnaby, D., & Thronson, H. A. 1992, AJ, 103, 41
Chen, J.-S., et al. 1999, in preparation
Fan, X.-H., et al. 1996, AJ, 112, 628
James, P., & Casali, M. M. 1998, MNRAS, 301, 280
Lasker, B. M., Sturch, C. R., McLean, B. J., Russell, J. L., Jenkner, H., & Shara, M. M. 1990, AJ, 99, 2019
Lequeux, J., Combes, F., Dantel-Fort, M., Cuillandre, J.-C., Fort, B., & Mellier, Y. 1998, A&A, 334, L9
Lequeux, J., Fort, B., Dantel-Fort, M., Cuillandre, J.-C., & Mellier, Y. 1996, A&A, 312, L1
Morrison, H. L., Boroson, T. A., & Harding, P. 1994, AJ, 108, 1191 (MBH)
Oke, J. B., & Gunn, J. E. 1983, ApJ, 266, 713
Peterson, R. C., Dalle Ore, C. M., & Kurucz, R. L. 1993, ApJ, 404, 333
Rudy, R. J., Woodward, C. E., Hodge, T., Fairfield, S. W., & Harker, D. E. 1997, Nature, 387, 159
Sackett, P. D., Morrison, H. L., Harding, P., & Boroson, T. A. 1994, Nature, 370, 441
Sancisi, R. 1976, A&A, 53, 159
Sasaki, T. 1987, PASJ, 39, 849
Shang, Z.-H., et al. 1998, ApJ, 504, L23
Skrutskie, M. F., Shure, M. A., & Beckwith, S. 1985, ApJ, 299, 303
Stetson, P. B. 1987, PASP, 99, 191
———. 1990, PASP, 102, 932
Tonry, J. L., Ajhar, E. A., & Luppino, G. A. 1990, AJ, 100, 1416
Tonry, J., & Schneider, D. P. 1988, AJ, 96, 807
van der Kruit, P. C. 1979, A&AS, 38, 15
van der Kruit, P. C., & Searle, L. 1981, A&AS, 95, 105
Wild, W. J. 1997, PASP, 109, 1269